Linear and nonlinear instability waves in spatially developing two-phase mixing layers

Lawrence C. Cheung and Tamer A. Zaki
Department of Mechanical Engineering, Imperial College London, London SW7 2AZ, United Kingdom

(Received 27 July 2009; accepted 13 April 2010; published online 21 May 2010)

Two-phase laminar mixing layers are susceptible to shear-flow and interfacial instabilities, which originate from infinitesimal disturbances. Linear stability theory has successfully described the early stages of instability. In particular, parallel-flow linear analyses have demonstrated the presence of mode competition, where the dominant unstable mode can vary between internal and interfacial modes, depending on the flow parameters. However, the dynamics of two-phase mixing layers can be sensitive to additional factors, such as the spreading of the mean flow. In addition, beyond the early linear stage, the amplitude of the instability waves becomes finite and nonlinear effects become appreciable. As a result, an accurate description of the evolution of the mixing layer must account for nonlinear interactions including the generation of higher harmonics of the instability waves and the modification of the mean flow. These effects are investigated herein using the framework of the nonlinear parabolized stability equations. The formulation includes nonparallel effects, nonlinear modal interactions, a coupled mean flow correction, and finite amplitude deformation of the interface. Mode competition between liquid and interfacial modes is investigated. We demonstrate that nonparallelism and streamwise evolution of the flow can significantly alter the predictions of locally parallel, linear stability analyses. This is followed by a discussion on nonlinear interactions of two- and three-dimensional instability waves. It is shown that nonlinear effects can serve dual purposes. On one hand, they can be a limiting mechanism for the growth of instability waves. On the other hand, they can destabilize high frequency, linearly stable modes, and thus lead to the generation of smaller scale features in the flow. © *2010 American Institute of Physics*. [doi:10.1063/1.3425788]

I. INTRODUCTION

The mechanics of two-fluid shear flows is significant in many engineering applications, where the growth of the interface is the primary consideration. For example, the instability of two-fluid flows affects the aerodynamic lift of airfoils in the presence of wall films such as deicing agents, the heat transfer rates of sheared film flows, and the breakup of capillary jets. Apart from direct numerical simulation (DNS), the majority of investigations to date have relied on linear or weakly nonlinear analyses of the two-fluid instability problem. The nonlinear behavior of these instability waves has not, however, been extensively investigated. In the current work, we employ a nonlinear formulation based on the parabolized stability equation (PSE) approach in order to study the evolution of disturbance waves in spatially developing, two-fluid, laminar mixing layers. With this framework we are able to show how nonlinearity and mean flow modifications can significantly alter the growth of instability modes.

Linear stability theory (LST) has led to the discovery of a wealth of possible instability mechanisms in two-fluid shear flows. Some of these mechanisms are associated with the mean shear, while others are attributed to the presence of the two-fluid interface. The original work of Miles[1,2] identified the critical layer mechanism in the study of wave generation by wind. Yih[3] demonstrated the existence of a long wavelength interfacial instability, which is entirely due to the viscosity discontinuity between the two fluids. Also, within the class of interfacial modes is a short-wavelength instability, which was discovered by Hooper and Boyd[4] and later explained by Hinch,[5] Renardy and Joseph,[6,7] and Yiantsios and Higgins.[8] Finally, at high shear rates, a short-wavelength liquid mode emerges.[9] Another classification of two-fluid instabilities was proposed by Boomkamp and Miesen.[10] They carried out a detailed analysis of the perturbation energy budget, similar to the analysis of Hu and Joseph,[11] and distinguished instability mechanisms based on the energy transfer from the mean flow to the disturbance.

In light of the wealth of possible instabilities, the notion of mode competition was discussed by Yecko *et al.*[12] They investigated the instability of laminar, two-fluid mixing layers and highlighted a shift of the most dominant instability from interfacial to liquid modes at low frequency. In that work, the growth rate of each mode was considered individually. The potential for energy amplification due to nonmodal effects was investigated by Yecko and Zaleski.[13] Their transient growth analysis follows the methodology originally used by South and Hooper[14] and van Noorden *et al.*[15] for bounded two-fluid flows.

All of the above studies exist within the context of linear theory and are therefore applicable only at the early stage development of the wave. Interactions between instability waves are typically ignored by these theories, and the development of the mean flow is also assumed to be independent

of the growth of the disturbances. In order to account for some of this phenomenology, a number of weakly nonlinear theories for two-phase flows have been proposed.[16–19] The majority of these formulations are based on the Stuart–Landau, Ginzburg–Landau, or Kuramoto–Sivashinsky equations. For marginally unstable instability waves near the bifurcation point, Stuart–Landau and Ginzburg–Landau theories allow an instability wave amplitude equation to be developed which accounts for a limited set of nonlinear interactions. King and McCready built upon the Stuart–Landau theory of Sangalli *et al.*[20,21] to include cubic and quadratic modal interactions in two-fluid bounded flows. As a result, they encountered situations where instability waves grew to a steady-state amplitudes due to energy transfer to higher frequency linearly stable modes. For small wavenumber, long-wave disturbances, the Kuramoto–Sivashinsky equation allows the temporal evolution of the wave amplitude to be captured. Formulations based on this theory have been used to study the effect of harmonic forcing in channel flows[18] and uncovered the existence of a mean flow shift.

Experimental studies have confirmed some aspects of weakly nonlinear theory. For instance, the work of Khomami and Su[22] and Khomami *et al.*[23] verified that linear theory could accurately describe the initial dynamics of interfacial instabilities. However, up to this point, most studies have focused on temporally growing disturbances in fully developed channel or pipe flows. This ignores some flows where the evolving mean flow can also lead to dampening of instabilities, such as two-fluid boundary layers or mixing layers. In addition, weakly nonlinear theories are generally valid only in the long wavelength limit or near the bifurcation point. These limitations exclude their application to spatially developing flows with strongly amplified instability waves.

An alternative approach to accurately predicting nonlinear instabilities in two-phase flow is DNS of the Navier–Stokes equations. Early work by Lombardi *et al.*[24] has considered a flat interface in turbulent shear flows. Later efforts, for example, the work of Fulgosi *et al.*,[25] have accounted for interface deformation using boundary conforming grids. Currently, DNS capabilities can track the evolution of the disturbance wave from its initial generation to ligament and droplet formation.[26–29] In order to account for complex deformations of the interface, accurate interface tracking schemes have been developed, such as volume of fluid,[30] level set,[31,32] or diffuse interface[33] methods. These methods, while very capability enabling, also present "severe numerical challenges"[34] when scaling to real-world problems. Due to their computational cost, DNS has been reserved for the study of a spectrum of perturbations interacting with an interface, i.e., turbulent flows.

Stability theory has continued to provide valuable insight into the early dynamics of two-fluid shear flows. Such insight is not easily extracted from direct computations of the Navier–Stokes equations, which are also computationally prohibitive for examining all possible stability mechanisms. Therefore, in this paper we develop an efficient and accurate nonlinear instability wave formulation to study finite amplitude disturbances in spatially developing, two-phase shear flows. Our approach extends the PSE framework introduced by Bertolotti *et al.*[35] Originally used in the study of boundary layer transition, the PSE since been applied to complex geometry,[36] aeroacoustics,[37] combustion,[38] and other applications. The nonlinear two-phase PSE formulation described herein provides a means to track the evolution of instability waves and the interface. It also consistently incorporates the effects of nonparallelism, nonlinearity, and mean flow distortions.

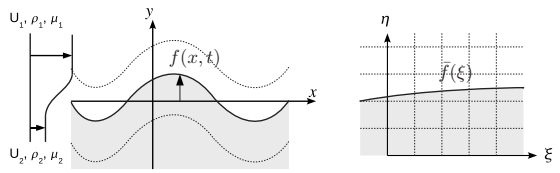

(a) Physical configuration (b) Mapped configuration

FIG. 1. Schematic of a two-fluid incompressible mixing layer in the (a) physical (x,y) coordinate system and (b) transformed (ξ,η) coordinates.

Our work seeks to address several open questions regarding the effects of nonparallelism and nonlinearity in the context of laminar two-fluid mixing layers. For instance, the phenomena of mode competition between liquid and interfacial instabilities have been studied by Yecko *et al.*[12] using parallel linear stability analysis. The nature of this competition is unknown in a spatially developing flow and is herein investigated. Also, by comparing the results from both linear and nonlinear stability computations, we demonstrate the effects of modal interactions and finite interface deformations on the growth of instability waves. We also demonstrate the modification of the mean flow due to finite amplitude disturbances.

The discussion of our work proceeds in the following order. In Sec. II, we present the formulation of the nonlinear stability equations. This framework is applied to the problem of mode competition in Sec. III. A comparison of several linear and nonlinear two-phase mixing layers is presented in Sec. IV. In Sec. V we discuss the effects of individual nonlinear mechanisms on the dynamics of the interfacial wave. Finally, the summary and conclusions of our work are given in Sec. VI.

II. METHODOLOGY

A. Governing equations

As shown in Fig. 1, we begin the analysis by considering a two-dimensional incompressible laminar mixing layer composed of two immiscible fluids. The velocities **u**, density ρ, and viscosity μ of this system can be identified with either the upper fluid or lower fluid using the subscript 1 (upper) or 2 (lower) where necessary. The free-stream velocities in the upper and lower fluid are given by U_1 and U_2, respectively. Furthermore, all variables used in this study have been nondimensionalized by the velocity U_1, initial shear layer vorticity thickness δ_0, and material properties of the upper stream. Thus, the density and viscosity of the upper stream are given by $\rho_1=\mu_1=1$, and the lower stream values are defined by the ratios $\rho_r=\rho_2/\rho_1$ and $\mu_r=\mu_2/\mu_1$. The Navier–Stokes equations governing such a system can be written as

$$\nabla \cdot \mathbf{u} = 0, \tag{1a}$$

$$\rho \frac{\mathrm{D}\mathbf{u}}{\mathrm{D}t} = -\nabla P + \frac{\mu}{\mathrm{Re}} \nabla^2 \mathbf{u} \tag{1b}$$

with the Reynolds number $\mathrm{Re} = \rho_1 U_1 \delta_0 / \mu_1$. In addition, the velocity $\mathbf{u}$ and stress tensor $\boldsymbol{\tau}$ for the two fluids must satisfy interfacial conditions applied at the location $y = f(x,z,t)$,

$$[\![\mathbf{u} \cdot \hat{\mathbf{n}}]\!] = 0, \quad [\![\mathbf{u} \cdot \hat{\mathbf{t}}]\!] = 0, \tag{2a}$$

$$[\![\boldsymbol{\tau} \cdot \hat{\mathbf{n}}]\!] = [\![P]\!]\hat{\mathbf{n}} - \sigma\kappa\hat{\mathbf{n}}, \quad [\![\boldsymbol{\tau} \cdot \hat{\mathbf{t}}]\!] = 0, \tag{2b}$$

where $\hat{\mathbf{n}}$ and $\hat{\mathbf{t}}$ denote the unit normal and tangent vectors to the interface, respectively, σ is the surface tension coefficient, κ is the interfacial curvature, and $[\![\bullet]\!]$ signifies a jump across the fluid boundary: $[\![q]\!] = q|_{y=f^+} - q|_{y=f^-}$. As discussed in Sec. II B, the mean pressure difference across the interface $[\![\bar{P}]\!]$ can be neglected when constructing the mean interfacial conditions, but the jump in perturbation pressure $[\![\tilde{p}]\!]$ must be considered. In the formulation presented below, we show how these conditions can be enforced exactly at the interface location and not at the nominal interface height, as in linear theory. Using these definitions, the Weber number can be written as $\mathrm{We} = \rho_1 U_1^2 \delta_0 / \sigma$. In addition, the interface location $f(x,z,t)$ is governed by the evolution equation

$$\frac{\mathrm{D}f}{\mathrm{D}t} = v. \tag{2c}$$

For subsonic mixing layers where the ratio $U_2/U_1 > 0$, the instability waves which propagate through the system are convectively unstable throughout the entire domain.[39] Therefore, tracking the evolution of the interfacial instability wave will require a *spatial* stability formulation and also require capturing the downstream spreading of the mean flow.

By decomposing the vector of flow variables $\phi = [u \;\; v \;\; w \;\; P]^T$ into a time-independent mean $\bar{\phi}$ and perturbation component $\tilde{\phi}$,

$$\phi = \bar{\phi}(x,y) + \tilde{\phi}(x,y,z,t), \tag{3}$$

where $\tilde{\phi}$ possesses zero time average, i.e., $\bar{\tilde{\phi}} = 0$, the solution of Eqs. (1) and (2) proceeds in two stages. The mean flow variables $\bar{\phi}$ are determined by solving the forced boundary layer approximation of the Navier–Stokes equations; the perturbation components $\tilde{\phi}$ are determined using the PSE formulation. The solutions of the two components are coupled through the nonlinear forcing terms that arise from higher order terms in $\tilde{\phi}$. A similar decomposition for the interface location $f(x,z,t) = \bar{f}(x,z) + \tilde{f}(x,z,t)$ ensures that large amplitude interface deformations are also handled consistently between the mean flow and the perturbation solutions. At the inlet, the mixing layer is harmonically forced using a spectrum of time varying, linearly unstable, discrete instability waves.

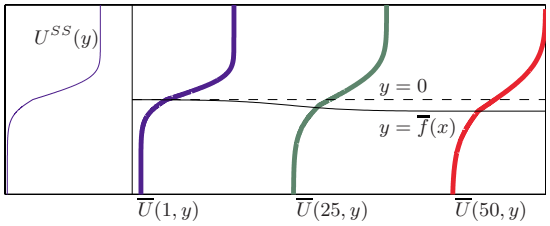

FIG. 2. (Color online) Schematic of spatially evolving mean flow, showing the inlet velocity profile $U^{SS}(y)$, mean velocity profile $\bar{U}(x,y)$ at $x = 1, 25, 50$, and the deviation of mean interface location $y = \bar{f}(x)$ away from $y = 0$.

B. The mean flow equation

Although many choices of the mean flow components $\bar{\phi} = [\bar{U} \;\; \bar{V} \;\; 0 \;\; \bar{P}]^T$ are available for a two-fluid mixing layer, few choices are suitable for the purposes of this study. The mean flow profiles should account for the spreading nature of the mean flow, changes to the mean interface location, and also be able to accommodate corrections arising from the interactions with the disturbance components (see Fig. 2). This prohibits the use of simpler choices such as the analytic profiles used by Yecko *et al.*,[12] or the self-similar mixing layer. While the self-similar mixing layer accounts for the spreading of the mean flow, it does not allow for any change to the mean interface location.

In this work, we adopt a more general approach and calculate the mean flow profile using as slightly modified version of the two-fluid boundary layer equations. The solution to these boundary layer equations is coupled to the solution of the perturbation components of flows, with the added advantage that both solutions can be solved in a parabolic manner (see Sec. II C 2). In the following discussion, we present the derivation of the mean flow equations, as well as the appropriate boundary conditions and solution method.

The governing equations for the mean flow components $\bar{\phi}$ can be derived by substituting the decomposition (3) into the Navier–Stokes equations (3) and applying a time average. Because the perturbation components possess zero time average, terms which are first order in $\tilde{\phi}$ are eliminated. Following the standard boundary layer observations that changes in the cross-stream direction are larger than in the streamwise direction, several approximations are then applied to simplify the mean equations. The streamwise and cross-stream pressure gradients are negligible, as are the second derivative terms $\partial^2/\partial x^2$. The $\bar{V}$ momentum equation can also be eliminated, resulting in the following equations for the mean flow:

$$\frac{\partial \bar{U}}{\partial x} + \frac{\partial \bar{V}}{\partial y} = 0, \tag{4a}$$

$$\rho \bar{U} \frac{\partial \bar{U}}{\partial x} + \rho \bar{V} \frac{\partial \bar{U}}{\partial y} - \frac{\mu}{\mathrm{Re}} \frac{\partial^2 \bar{U}}{\partial y^2} = F_{x,BL}, \tag{4b}$$

$$\frac{D\bar{f}}{Dt} = \bar{V}. \tag{4c}$$

The nonlinear term $F_{x,BL}$ on the right hand side of Eq. (4b) arises from quadratic and higher order terms in $\tilde{\phi}$, which can be of finite amplitude and can possess a nonzero mean (see Sec. II C 2).

At the cross-stream boundaries, the velocities should approach their free-stream values,

$$\bar{U}(y=\infty) = U_1, \quad \bar{U}(y=-\infty) = U_2, \quad \bar{V}(y=\infty) = V_1^{SS}, \tag{5a}$$

$$\bar{V}(y=-\infty) = V_2^{SS},$$

and the initial profile at $x=0$ is given by

$$\bar{U}(x=0,y) = U^{SS}(y). \tag{5b}$$

Both the initial profile $U^{SS}(y)$ and the boundary conditions $V_{1,2}^{SS}$ at $y=\pm\infty$ are found from the self-similar solution of the laminar two-fluid mixing layer, which is fully described in Appendix A and by White.[40] Because large disturbances caused by the perturbations appear far downstream and are confined to the sheared region of the flow, they have little effect on the mean flow at the inlet and in the free stream. Thus, the self-similar solution can be applied at the inlet and as boundary conditions at $y=\pm\infty$. At the inlet location $x=x_0$, the velocity profile is chosen such that the vorticity thickness $\delta_\omega(x_0)=\delta_0=1$.

A set of mean interface conditions, which are consistent with the mean flow equations (4), can be derived by taking the time average of Eq. (3) and assuming all variables can be separated into mean and fluctuating components. Hence, the interfacial velocity conditions

$$\langle [\![\mathbf{u}\cdot\hat{\mathbf{n}}]\!] \rangle = 0, \quad \langle [\![\mathbf{u}\cdot\hat{\mathbf{t}}]\!] \rangle = 0,$$

where $\langle \bullet \rangle$ indicates time averaging, yield the time-independent conditions

$$[\![\bar{U}]\!] = 0, \quad [\![\bar{V}]\!] = 0. \tag{6a}$$

A similar time average of the stress conditions gives

$$\langle [\![\bar{\boldsymbol{\tau}}\cdot\hat{\mathbf{n}}]\!] \rangle = [\![\bar{P}]\!] - \sigma\bar{\kappa}, \quad \langle [\![\bar{\boldsymbol{\tau}}\cdot\hat{\mathbf{t}}]\!] \rangle = 0,$$

where the mean stress tensor $\bar{\tau}_{ij} = \mu(\partial\bar{U}_i/\partial x_j + \partial\bar{U}_j/\partial x_i)$ and the curvature $\kappa = \bar{\kappa}(\mathbf{x}) + \tilde{\kappa}(\mathbf{x},t)$. The slowly evolving nature of the spatial mixing layer implies that the mean curvature $\bar{\kappa}$ remains small. Indeed, computations of $\bar{\kappa}$ for the mixing layers of interest indicate it is of the order $O(10^{-5})$ and can be safely neglected. Additionally, the *mean* normal of the interface remains close to $\bar{\mathbf{n}} = (0,1,0)$. After applying the condition that $[\![\bar{P}]\!] = 0$ and the boundary layer approximation that $\partial\bar{V}/\partial x$ is of the order of $O(\mathrm{Re}^{-1})$ smaller than $\partial\bar{U}/\partial y$ in $\bar{\tau}_{xy}$, the final result for the stress conditions are

$$\left[\!\!\left[\mu\frac{\partial\bar{U}}{\partial y} \right]\!\!\right] = 0, \quad \left[\!\!\left[\mu\frac{\partial\bar{V}}{\partial y} \right]\!\!\right] = 0. \tag{6b}$$

Note that the interfacial conditions (6a) and (6b) are applied at the mean interface location $y=\bar{f}$. Through the use of the coordinate mapping discussed in Sec. II C 1, we find that the perturbation interfacial conditions can also be applied at the same location. These interfacial conditions for the perturbation variables are given in Sec. II C 2.

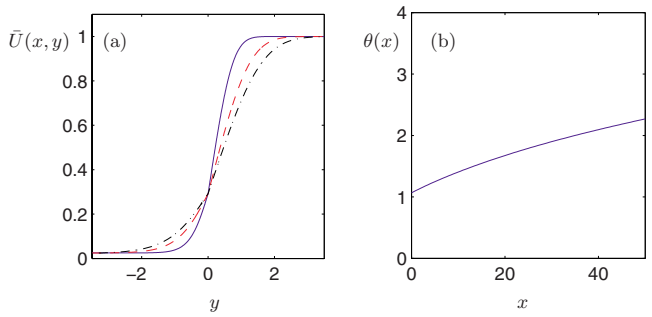

FIG. 3. (Color online) (a) The mean velocity profile $\bar{U}(x,y)$ at different streamwise positions: $x=0$ (—), $x=25$ (--), and $x=50$ (−·−). (b) The momentum thickness $\theta(x)$. The mixing layer parameters are given by $U_2/U_1=0.03$, $\rho_r=10$, and $\mu_r=2$.

The solution to the mean flow is found by solving Eq. (4) with conditions (5) and (6). This solution is advanced downstream from the inlet using a Crank–Nicolson scheme with fourth order central differencing in y, similar to algorithms presented in Ref. 41. Accounting for the mean flow correction, however, introduces an additional complication to the standard boundary layer solution. The downstream marching must be synchronized with the PSE solution to allow for the exchange of mean flow information and forcing terms $F_{x,BL}$, which is calculated in the process of solving the stability modes.

The evolution of the streamwise velocity profile $\bar{U}(y)$ for a typical mixing layer, with parameters $U_2/U_1=0.03$, $\rho_r=10$, and $\mu_r=2$, is shown below in Fig. 3(a). The width of the mixing layer, as defined by the momentum thickness

$$\theta(x) = \int_{-\infty}^{\infty} \rho\left[\frac{\bar{U}(y)-U_2}{U_1-U_2}\right]\left[1-\frac{\bar{U}(y)-U_2}{U_1-U_2}\right]dy,$$

is plotted in Fig. 3(b). For the mixing layers used in this study, the typical spreading rate was relatively small, on the order of $d\theta/dx \approx 0.025$ in this particular case.

C. The perturbation equations

By inserting the using the decomposition (3) in the Navier–Stokes equations and removing the time-independent base flow components $\bar{\phi}$, the equations governing the perturbation variables $\tilde{\phi} = [\tilde{u}\ \tilde{v}\ \tilde{w}\ \tilde{p}]^T$ can be written as

$$\boldsymbol{\nabla}\cdot\tilde{\mathbf{u}} = 0, \tag{7a}$$

$$\rho\left[\frac{\partial\tilde{\mathbf{u}}}{\partial t} + (\tilde{\mathbf{u}}\cdot\boldsymbol{\nabla})\bar{\mathbf{U}} + (\bar{\mathbf{U}}\cdot\boldsymbol{\nabla})\tilde{\mathbf{u}}\right] + \boldsymbol{\nabla}\tilde{p} - \frac{\mu}{\mathrm{Re}}\boldsymbol{\nabla}^2\tilde{\mathbf{u}} = -\rho\tilde{\mathbf{u}}\cdot\boldsymbol{\nabla}\tilde{\mathbf{u}}, \tag{7b}$$

$$\frac{D\tilde{f}}{Dt} = \tilde{v}, \tag{7c}$$

along with the appropriate interfacial conditions imposed at $y=f(x,t)$. Note that Eq. (7b) remains an exact rearrangement of the momentum equation (1b) for the perturbation velocity $\tilde{u}$, and no assumptions have been made so far regarding the perturbations $\tilde{\phi}$ other than its time dependence. In this study, we emphasize the role of nonlinear and finite amplitude effects, which prohibits making any small-amplitude or linearizing assumptions where $|\tilde{\phi}|/|\bar{\phi}| \ll 1$. As we describe in Secs. II C 1 and II C 2, the solution to Eq. (7) is found by first transforming to a coordinate system following the interfacial wave and then parabolizing the system according to the PSE formulation.

1. Coordinate transformation

In order to account for the effects of the finite deformation of the interface, the interfacial conditions (2a) and (2b) should always be applied at the physical location $y=f(x,z,t)$ and not about a linearized location at $y=0$. However, imposing the conditions at the time dependent wave height $f(x,z,t)$ presents additional difficulties when attempting to use a frequency domain representation for the disturbance components $\tilde{\phi}$. By using a coordinate transformation to map the physical domain to a computational domain where the interface is static, we can avoid these difficulties in enforcing the interface conditions,

$$\begin{aligned} \tau &= t, \\ \xi &= x, \\ \eta &= y - H(\xi,\eta,\zeta,\tau), \\ \zeta &= z. \end{aligned} \tag{8}$$

In the mapped coordinates (8), the interface is permanently located at $\eta=\bar{f}(\xi,\zeta)$ (see Fig. 1), and the coordinate mapping function H satisfies the condition $H(\xi,\eta=\bar{f},\zeta,\tau)=\tilde{f}(x,z,t)$. Therefore, the instantaneous interface location $y=\bar{f}+\tilde{f}$ is always mapped to $\eta=\bar{f}$. We note that this coordinate transform does not allow for a multivalued interface deformation [$f(x,z,t)$ and $H(\xi,\eta,\zeta,\tau)$ are required to be single valued]. Hence, although large amplitude interface deformations can occur, the coordinate mapping precludes the two-phase system from cresting or undergoing vortex roll-up. The exact form of $H(\xi,\eta,\zeta,\tau)$ will be discussed in Sec. II C 2.

From the coordinate transformation given by Eq. (8), the derivatives in physical space are transformed according to the following expressions:

$$\begin{aligned} \frac{\partial}{\partial t} &= \frac{\partial}{\partial \tau} + g_\tau \frac{\partial}{\partial \eta}, \quad \frac{\partial}{\partial x} = \frac{\partial}{\partial \xi} + g_\xi \frac{\partial}{\partial \eta}, \\ \frac{\partial}{\partial y} &= \frac{\partial}{\partial \eta} + g_\eta \frac{\partial}{\partial \eta}, \quad \frac{\partial}{\partial z} = \frac{\partial}{\partial \zeta} + g_\zeta \frac{\partial}{\partial \eta}, \end{aligned} \tag{9}$$

where the coefficients are given by

$$g_\tau = \frac{-\frac{\partial H}{\partial \tau}}{1+\frac{\partial H}{\partial \eta}}, \quad g_\xi = \frac{-\frac{\partial H}{\partial \xi}}{1+\frac{\partial H}{\partial \eta}},$$

$$g_\eta = \frac{1}{1+\frac{\partial H}{\partial \eta}} - 1, \quad g_\zeta = \frac{-\frac{\partial H}{\partial \zeta}}{1+\frac{\partial H}{\partial \eta}}.$$

Using the derivative transforms (9) in Eq. (7) allows us to write the perturbation equations in a coordinate system following the interfacial wave and also eliminates the need to carry a separate Eq. (7c) to track the location of the interface. In this coordinate system, the complete equations for mass and momentum conservation (7a) and (7b) can be written as

$$\frac{\partial \tilde{u}}{\partial \xi} + \frac{\partial \tilde{v}}{\partial \eta} + \frac{\partial \tilde{w}}{\partial \zeta} = -g_\xi\left(\frac{\partial \bar{U}}{\partial \eta} + \frac{\partial \tilde{u}}{\partial \eta}\right) - g_\eta\left(\frac{\partial \bar{V}}{\partial \eta} + \frac{\partial \tilde{v}}{\partial \eta}\right) - g_\zeta\left(\frac{\partial \tilde{w}}{\partial \eta}\right), \tag{10a}$$

$$\begin{aligned} &\rho\left[\frac{\partial \tilde{u}}{\partial \tau} + \bar{U}\frac{\partial \tilde{u}}{\partial \xi} + \tilde{u}\frac{\partial \bar{U}}{\partial \xi} + \bar{V}\frac{\partial \tilde{u}}{\partial \eta} + \tilde{v}\frac{\partial \bar{U}}{\partial \eta}\right] + \frac{\partial \tilde{p}}{\partial \xi} - \mu\nabla^2_{(\xi,\eta,\zeta)}\tilde{u} \\ &= -\rho\left[\tilde{u}\frac{\partial \tilde{u}}{\partial \xi} + \tilde{v}\frac{\partial \tilde{u}}{\partial \eta} + \tilde{w}\frac{\partial \tilde{u}}{\partial \zeta}\right] - g_\xi\frac{\partial \tilde{p}}{\partial \eta} \\ &\quad - \rho[g_\tau + (\bar{U}g_\xi + \bar{V}g_\eta) + (\tilde{u}g_x + \tilde{v}g_y + \tilde{w}g_z)]\frac{\partial}{\partial \eta}(\bar{U}+\tilde{u}) \\ &\quad + \frac{2\mu}{\mathrm{Re}}\left[g_\xi\frac{\partial^2 \tilde{u}}{\partial \xi\,\partial \eta} + g_\eta\frac{\partial^2}{\partial \eta^2}(\bar{U}+\tilde{u}) + g_\zeta\frac{\partial^2 \tilde{u}}{\partial \eta\,\partial \zeta}\right] \\ &\quad + \frac{\mu}{\mathrm{Re}}\left[g_\gamma\frac{\partial}{\partial \eta}(\bar{U}+\tilde{u}) + g^2\frac{\partial^2}{\partial \eta^2}(\bar{U}+\tilde{u})\right], \end{aligned} \tag{10b}$$

$$\begin{aligned} &\rho\left[\frac{\partial \tilde{v}}{\partial \tau} + \bar{U}\frac{\partial \tilde{v}}{\partial \xi} + \tilde{u}\frac{\partial \bar{V}}{\partial \xi} + \bar{V}\frac{\partial \tilde{v}}{\partial \eta} + \tilde{v}\frac{\partial \bar{V}}{\partial \eta}\right] + \frac{\partial \tilde{p}}{\partial \eta} - \mu\nabla^2_{(\xi,\eta,\zeta)}\tilde{v} \\ &= -\rho\left[\tilde{u}\frac{\partial \tilde{v}}{\partial \xi} + \tilde{v}\frac{\partial \tilde{v}}{\partial \eta} + \tilde{w}\frac{\partial \tilde{v}}{\partial \zeta}\right] - g_\eta\frac{\partial \tilde{p}}{\partial \eta} \\ &\quad - \rho[g_\tau + (\bar{U}g_\xi + \bar{V}g_\eta) + (\tilde{u}g_x + \tilde{v}g_y + \tilde{w}g_z)]\frac{\partial}{\partial \eta}(\bar{V}+\tilde{v}) \\ &\quad + \frac{2\mu}{\mathrm{Re}}\left[g_\xi\frac{\partial^2 \tilde{v}}{\partial \xi\,\partial \eta} + g_\eta\frac{\partial^2}{\partial \eta^2}(\bar{V}+\tilde{v}) + g_\zeta\frac{\partial^2 \tilde{v}}{\partial \eta\,\partial \zeta}\right] \\ &\quad + \frac{\mu}{\mathrm{Re}}\left[g_\gamma\frac{\partial}{\partial \eta}(\bar{V}+\tilde{v}) + g^2\frac{\partial^2}{\partial \eta^2}(\bar{V}+\tilde{v})\right], \end{aligned} \tag{10c}$$

$$\rho\left[\frac{\partial\tilde{w}}{\partial\tau}+\bar{U}\frac{\partial\tilde{w}}{\partial\xi}+\bar{V}\frac{\partial\tilde{w}}{\partial\eta}\right]+\frac{\partial\tilde{p}}{\partial\zeta}-\mu\nabla^2_{(\xi,\eta,\zeta)}\tilde{w}$$
$$=-\rho\left[\tilde{u}\frac{\partial\tilde{w}}{\partial\xi}+\tilde{v}\frac{\partial\tilde{w}}{\partial\eta}+\tilde{w}\frac{\partial\tilde{w}}{\partial\zeta}\right]$$
$$-\rho[g_\tau+(\bar{U}g_\xi+\bar{V}g_\eta)+(\tilde{u}g_x+\tilde{v}g_y+\tilde{w}g_z)]\frac{\partial}{\partial\eta}(\bar{W}+\tilde{w})$$
$$+\frac{2\mu}{\mathrm{Re}}\left[g_\xi\frac{\partial^2\tilde{w}}{\partial\xi\,\partial\eta}+g_\eta\frac{\partial^2\tilde{w}}{\partial\eta^2}+g_\zeta\frac{\partial^2\tilde{v}}{\partial\eta\,\partial\zeta}\right]$$
$$+\frac{\mu}{\mathrm{Re}}\left[g_\gamma\frac{\partial\tilde{w}}{\partial\eta}+g^2\frac{\partial^2\tilde{w}}{\partial\eta^2}\right], \tag{10d}$$

using the following definitions for the Laplacian $\nabla^2_{(\xi,\eta,\zeta)}$ and g_γ, g^2 factors:

$$\nabla^2_{(\xi,\eta,\zeta)}=\frac{\partial^2}{\partial\xi^2}+\frac{\partial^2}{\partial\eta^2}+\frac{\partial^2}{\partial\zeta^2},\quad g_\gamma=\frac{\partial g_\xi}{\partial\xi}+\frac{\partial g_\eta}{\partial\eta}+\frac{\partial g_\zeta}{\partial\zeta},$$

$$g^2=g_\xi^2+g_y^2+g_\zeta^2.$$

2. Nonlinear instability wave formulation

For a convectively unstable, slowly evolving mean flow, Bertolotti *et al.*[35] showed that it was possible to parabolize the perturbation equations (7) and reduce them to a system which can be marched downstream to track the streamwise evolution of instability waves. This approach has been previously applied to single-phase mixing layers, jets, and boundary layers and is extended here to the two-phase problem. The methodology presented below is analogous to the PSE formulation used in Cheung and Lele,[42] although several differences are noted below.

The physical observation which underlies PSE theory is that the spatial variations of the mean flow occur on a much longer scale (L) than the wavelength (λ) of a characteristic disturbance. Given these two disparate length scales in the problem, it is then possible to separate the disturbances into slowly and rapidly varying components. Streamwise changes to quantities such as the mode shape, wavelength, and growth rate are presumed to be small on the short length scale. These slowly varying assumptions can be verified *a posteriori*, as shown in Sec. II C 4.

In deriving the perturbation equations, we must emphasize that no linearization step has been employed, and we explicitly allow for the possibility that perturbations grow from small amplitude to finite amplitude disturbances. Hence, the utility of the nonlinear PSE (NPSE) formulation arises from the inclusion of nonlinear terms and its ability to capture finite amplitude effects.

The first major assumption in deriving the NPSE is the following normal mode representation for the disturbances:

$$\tilde{\phi}(\xi,\eta,\zeta,\tau)=\sum_{m,n}^{M,N}\hat{\phi}_{mn}(\xi,\eta)\mathcal{A}_{mn}(\xi)\exp\{i\beta_n\zeta-i\omega_m\tau\}, \tag{11}$$

where the amplitude factor $\mathcal{A}_{mn}(\xi)$ is written as

$$\mathcal{A}_{mn}(\xi)=\epsilon_{mn}\exp\left\{i\int_0^\xi\alpha_{mn}(\xi')d\xi'\right\}. \tag{12}$$

In Eqs. (11) and (12), an initial amplitude ϵ_{mn} is provided for each shape function $\hat{\phi}_{mn}$, which also corresponds with an associated streamwise wavenumber α_{mn}, spanwise wavenumber β_n, and temporal frequency ω_m. In contrast to parallel LST, both $\hat{\phi}_{mn}$ and α_{mn} are functions of the streamwise variable ξ.

The slow variation in $\tilde{\phi}$ and α in the streamwise direction translate to the following assumptions on the PSE system:

$$\frac{\partial^2}{\partial\xi^2}\hat{\phi}_{mn}(\xi)\ll O(1)\quad\text{and}\quad\frac{\partial^2}{\partial\xi^2}\alpha_{mn}(\xi)\ll O(1), \tag{13}$$

such that the second order derivatives can be neglected in comparison to the first order derivatives. In addition, the rate of evolution of the mean flow is assumed to be slow such that

$$\frac{1}{\mathrm{Re}}\frac{\partial\bar{\phi}}{\partial\xi}\ll O(1)\quad\text{and}\quad\frac{\partial^2\bar{\phi}}{\partial\xi^2}\ll O(1) \tag{14}$$

and can be neglected in the analysis as well.

In a similar manner, we can express $H(\xi,\eta,\zeta,\tau)$ from Eq. (8) using the modal expansion,

$$H(\xi,\eta,\zeta,\tau)=\sum_{m,n\neq0}^{M,N}\epsilon_{mn}\hat{h}_{mn}(\eta)$$
$$\times\exp\left\{i\int_0^\xi\alpha_{mn}(\xi')d\xi'+i\beta_n\zeta-i\omega_m\tau\right\}.$$

The frequencies ω_m and wavenumbers α_{mn}, β_n are chosen to correspond to the same frequencies and wavenumbers used in Eq. (11), and the functions $\hat{h}_{mn}(\eta)$ are chosen such that $\partial\hat{h}/\partial\eta=0$ at $\eta=\bar{f}$, and $\hat{h}(\eta)\to0$ as $\eta\to\pm\infty$. For the purposes of this formulation, $\hat{h}_{mn}(\eta)$ is taken to be a set of smooth functions in η, which decay exponentially away from the interface at the same rate as the linear stability eigenmodes. To satisfy the kinematic condition (7c) at the interface, we also require that

$$\hat{h}_{mn}(\eta=\bar{f})=\frac{\hat{v}_{mn}(\bar{f})}{i[\alpha_{mn}\bar{U}(\bar{f})-\omega_m]},$$

where $\hat{v}_{mn}$ is the vertical velocity shape function given by the PSE solution.

Inserting Eqs. (11) and (12) and the assumptions (13) and (14) into the perturbation equations (10) yields the following set of nonlinear disturbance equations:

$$i\alpha_{mn}\hat{u}_{mn}+\frac{\partial\hat{u}_{mn}}{\partial\xi}+\frac{\partial\hat{v}_{mn}}{\partial\eta}+i\beta_n\hat{w}=\mathcal{F}_{\rho,mn}, \tag{15a}$$

$$\rho\left[-i\omega_m + i\alpha_{mn}\bar{U} + \frac{\partial \bar{U}}{\partial \xi}\right]\hat{u}_{mn} + \rho\bar{V}\frac{\partial \hat{u}_{mn}}{\partial \eta} + \rho\frac{\partial \bar{U}}{\partial \eta}\hat{v}_{mn} + i\alpha_{mn}\hat{p}_{mn} + \frac{\mu}{\mathrm{Re}}\left(\alpha_{mn}^2 + \beta_n^2 - \frac{\partial^2}{\partial \eta^2}\right)\hat{u}_{mn} + [\rho\bar{U} - 2i\alpha_{mn}\mu]\frac{\partial \hat{u}_{mn}}{\partial \xi} + \Omega\frac{\partial \hat{p}_{mn}}{\partial \xi} - \mu i\frac{\partial \alpha_{mn}}{\partial \xi}\hat{u}_{mn} = \mathcal{F}_{x,mn}, \tag{15b}$$

$$\rho\left[-i\omega_m + i\alpha_{mn}\bar{U} + \frac{\partial \bar{V}}{\partial \eta}\right]\hat{v}_{mn} + \rho\bar{V}\frac{\partial \hat{v}_{mn}}{\partial \eta} + \rho\frac{\partial \bar{V}}{\partial \xi}\hat{u}_{mn} + \frac{\partial \hat{p}_{mn}}{\partial \eta} + \frac{\mu}{\mathrm{Re}}\left(\alpha_{mn}^2 + \beta_n^2 - \frac{\partial^2}{\partial \eta^2}\right)\hat{v}_{mn} + [\rho\bar{U} - 2i\alpha_{mn}\mu]\frac{\partial \hat{v}_{mn}}{\partial \xi} - \mu i\frac{\partial \alpha_{mn}}{\partial \xi}\hat{v}_{mn} = \mathcal{F}_{y,mn}, \tag{15c}$$

$$\rho[-i\omega_m + i\alpha_{mn}\bar{U}]\hat{w}_{mn} + \rho\bar{V}\frac{\partial \hat{w}_{mn}}{\partial \eta} + i\beta_n\hat{p} + \frac{\mu}{\mathrm{Re}}\left(\alpha_{mn}^2 + \beta_n^2 - \frac{\partial^2}{\partial \eta^2}\right)\hat{w} + [\rho\bar{U} - 2i\alpha_{mn}\mu]\frac{\partial \hat{w}_{mn}}{\partial \xi} - \mu i\frac{\partial \alpha_{mn}}{\partial \xi}\hat{w} = \mathcal{F}_{z,mn}, \tag{15d}$$

which form the basis for the NPSE method. The right hand side of Eq. (18) contains the nonlinear forcing functions $\mathcal{F}_{mn}$, which are composed of higher order products of the disturbances $\tilde{\phi}$ and the mapping function $H(\xi,\eta,\zeta,\tau)$. The zero-frequency forcing terms couple the perturbation equations to the mean flow equations (4), i.e., $F_{x,BL}=\mathcal{F}_{x,00}$.

In addition to Eq. (14), an additional normalization condition must be included to make Eq. (18) solvable. The need for this normalization condition arises from the form of the representation used in Eq. (11). Because both $\hat{\phi}_{mn}(\xi,\eta)$ and $\alpha_{mn}(\xi)$ are dependent on ξ, streamwise changes in $\tilde{\phi}$ can be absorbed into either variable. To remove this ambiguity in the representation, we apply the integral norm

$$\int_{-\infty}^{\infty}\rho\left(\hat{u}_{mn}\frac{\partial \hat{u}_{mn}}{\partial \xi} + \hat{v}_{mn}\frac{\partial \hat{v}_{mn}}{\partial \xi} + \hat{w}_{mn}\frac{\partial \hat{w}}{\partial \xi}\right)d\eta = 0. \tag{16}$$

Physically, this particular normalization condition can be interpreted as preserving the kinetic energy of the shape function components as the solutions are marched downstream. Although many different normalization conditions have been proposed,[35] the normalizations most typically used in literature adopt a similar form to Eq. (16) in order to limit any rapid changes from occurring in the shape functions.

When examining the results of PSE simulations, it should be noted that different choices of the normalization will lead to different streamwise changes in $\hat{\phi}$ and α. Therefore, comparisons between different types of simulations should involve quantities that account for this flexibility in the representation (11). This issue is addressed again in Sec. IV A, where the modal energy is defined and used in the comparison of linear and NPSE results.

An additional modification was also necessary to eliminate upstream propagating characteristics from destabilizing the PSE solution. Following the recommendations of Haj-Hariri,[43] the streamwise pressure derivative was modified in the x-momentum equation. This was accomplished by setting the control parameter $\Omega=0$ in Eq. (15a) and omitting the $\partial\hat{p}/\partial\xi$ derivative, resulting in the following expression for the pressure gradient in physical coordinates:

$$\frac{\partial \tilde{p}}{\partial \xi} = \sum_{m,n} i\alpha_{mn}\hat{p}_{mn}\mathcal{A}_{mn}(\xi)e^{i\beta_n z - i\omega_m t}.$$

Different choices for the parameter Ω and their implications are described in the analysis of Li and Malik.[44] To accommodate the change in phase at the interface, the interfacial conditions

$$[\![\hat{u}_{mn}]\!] = 0, \quad [\![\hat{v}_{mn}]\!] = 0, \quad [\![\hat{w}_{mn}]\!] = 0, \tag{17a}$$

$$\left[\!\!\left[-\hat{p}_{mn} + 2\mu\frac{\partial \hat{v}_{mn}}{\partial \eta}\right]\!\!\right] = -\frac{ik^2\hat{v}_{mn}}{\mathrm{We}M}, \quad \left[\!\!\left[\mu\left(\frac{\partial \hat{u}_{mn}}{\partial \eta} + i\alpha\hat{v}_{mn}\right)\right]\!\!\right] = 0 \tag{17b}$$

are applied for each shape function $\hat{\phi}_{mn}$ at location $\eta=\bar{f}$, and where $k^2=\alpha_{mn}^2+\beta_n^2$, and $M=\alpha_{mn}\bar{U}(\bar{f})-\omega$.

The final perturbation equations which we wish to solve can be written in operator form as

$$\mathcal{L}_{mn}\{\hat{\phi}_{mn}\} = \mathcal{F}_{mn}/\mathcal{A}_{mn}. \tag{18}$$

Using the matrices **A**, **B**, **C**, **D**, **E**, **G**, **M**, and **N** defined in Appendix B, the linear operator $\mathcal{L}_m$ can be expressed as

$$\mathcal{L}_{mn} = -i\omega_m\mathbf{G} + i\alpha_{mn}\mathbf{A} + \mathbf{B}\frac{\partial}{\partial \eta} + \mathbf{C}\frac{\partial^2}{\partial \eta^2} + i\beta_n\mathbf{D} + \mathbf{E} + \mathbf{M}\frac{\partial}{\partial \xi} + \frac{\partial \alpha_{mn}}{\partial \xi}\mathbf{N}. \tag{19}$$

The initial boundary and boundary conditions necessary to solve this parabolic problem are given by

$$\hat{\phi}_{mn} = \hat{\phi}_{mn}^{\mathrm{OS}}(\eta), \quad \alpha_{mn}(0) = \alpha_{mn}^{\mathrm{OS}} \quad \text{at} \quad \xi = 0, \qquad \hat{\phi}_{mn} \to 0 \quad \text{as} \quad \eta \to \pm\infty. \tag{20}$$

Along with the normalization condition (16) and interfacial conditions (17), Eqs. (18)–(20) define the two-fluid NPSE formulation used in this work. The linear PSE (LPSE) formulation can be recovered by setting $\mathcal{F}_{mn}=0$ and eliminating the forcing term $\bar{F}$ from the mean flow equation (4b).

At the start of the PSE simulations, the initial shape functions $\hat{\phi}_{mn}^{\mathrm{OS}}(\eta)$ and wavenumbers $\alpha_{mn}^{\mathrm{OS}}$ are provided by solutions to the Orr–Sommerfeld (OS) equations. These OS solutions are computed for a parallel mean flow given by $\bar{\mathbf{U}}=[\bar{U}(\xi=0,\eta),0,0]$, as detailed in Appendix C. A discrete set of forcing frequencies was chosen by selecting a fundamental mode ω_0 with an initially unstable growth rate at the

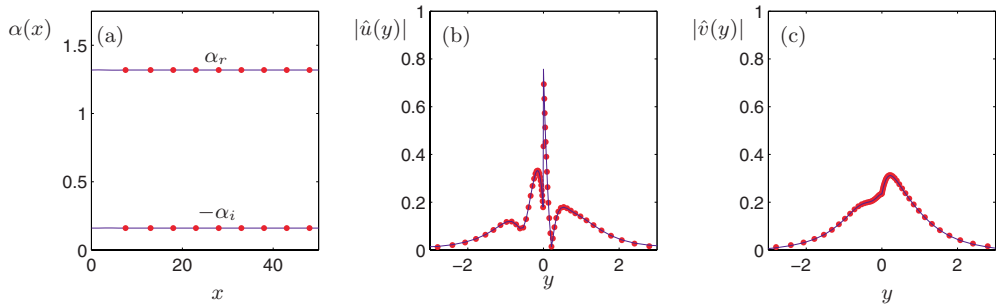

FIG. 4. (Color online) Validation of the LPSE for a two-phase mixing layer with $U_2/U_1=0.30$, $\rho_r=10$, $\mu_r=2$, We=300, and Re=150. The results of the parallel-flow LST are shown in dots (●), while the LPSE results at $x=12$ are shown in solid lines (—). (a) The wavenumber $\alpha_r(x)$ and growth rate $-\alpha_i(x)$, (b) the streamwise velocity shape function $|\hat{u}(y)|$, and (c) the cross-stream velocity shape function $|\hat{v}(y)|$.

inlet. The resulting Strouhal number for the fundamental frequency is then given by $\mathrm{St}_0=\omega_0\delta_0/(2\pi\Delta U)$. In addition, higher harmonics of this fundamental were also included at the frequencies $\omega_m=m\omega_0$ for integer values of m. Thus, the physical inlet perturbation can be written as

$$\tilde{\phi}(\xi=0,\eta,\zeta,\tau)=\sum_{m,n}\epsilon_{mn}\hat{\phi}_{mn}^{\mathrm{OS}}(\eta)e^{-im\omega_0\tau+i\beta_n\zeta}.$$

For all modes, the initial amplitudes ϵ_{mn} were generally less than 0.1% of the free-stream velocity.

Although the previous description of the NPSE formulation generally follows Cheung and Lele,[42] several distinct differences should be noted. Most noticeably, the two-phase incompressible nature of the current flow requires the addition of the coordinate mapping (8) and interfacial conditions (17). In addition, the compressible formulation of Cheung and Lele used a self-similar mean flow and corrected the mean flow via a zero frequency mode rather than forcing the boundary layer equations (4) directly. These changes are also reflected in the solution procedure discussed below.

3. Solution procedure

The computational methodology for solving perturbation equations (18) and (16) and mean flow equations (4) is similar to the numerical algorithms described in Refs. 38 and 42 and are summarized here for the sake of completeness. The NPSE (18) was discretized using the fourth order central differencing in η and advanced in the streamwise direction using the first order implicit Euler method. Therefore, if the operator (19) is written as $\mathcal{L}_{mn}=\mathbf{L}_{mn}+\mathbf{M}_{mn}(\partial/\partial\xi)+\mathbf{N}_{mn}(\partial\alpha_{mn}/\partial\xi)$, then the discretized form of Eq. (18) will become

$$[(\Delta\xi)\mathbf{L}_{mn}^{i+1}+\mathbf{M}_{mn}^{i+1}+(\alpha_{mn}^{i+1}-\alpha_{mn}^{i})\mathbf{N}_{m}^{i+1}]\hat{\phi}_{mn}^{i+1}=\mathbf{M}_{mn}^{i+1}\hat{\phi}_{mn}^{i}+\frac{\mathbf{F}_{mn}^{i+1}}{\mathcal{A}_{mn}^{i+1}}\Delta\xi. \quad (21)$$

Grid stretching in the cross-stream direction and a variable streamwise step size efficiently allocated grid points to locations where higher gradients were expected. The nonlinear terms $\mathcal{F}_{mn}$ were calculated in the time domain and Fourier transformed into the frequency domain before solving Eq. (21). The zero frequency nonlinear terms $\mathcal{F}_{00}$ in physical space were used as the nonlinear forcing term to the mean flow boundary layer equations (4).

In order to satisfy the normalization condition and Eq. (21) simultaneously, an iterative solution process was employed at each streamwise position. At a particular ξ^i and iteration level j, the mean flow equations (4) and the disturbance equation (21) for each mode were solved to obtain $\bar{\phi}^{i+1,j}$, $\bar{f}^{i+1,j}$, and $\hat{\phi}_{mn}^{i+1,j}$ at the next point ξ^{i+1}. The wavenumbers α_{mn}^{i+1} were updated at each iteration level by using a discretized form of the normalization condition

$$\alpha_{mn}^{i+1,j+1}=\alpha_{mn}^{i+1,j}-\frac{i}{\Delta\xi}\frac{\int\rho(\hat{\mathbf{u}}_{mn}^{i+1,j})^*\cdot(\hat{\mathbf{u}}_{mn}^{i+1,j}-\hat{\mathbf{u}}_{mn}^{i,j})d\eta}{\int\rho|\hat{\mathbf{u}}_{mn}^{i+1,j}|^2d\eta}. \quad (22)$$

The iteration process continued until the difference $|\alpha_{mn}^{i+1,j+1}-\alpha_{mn}^{i+1,j}|$ fulfilled a specified tolerance level, at which point the PSE solution was advanced to the next streamwise position. By solving both the mean flow equations and the disturbance equations simultaneously at each iteration level, a fully consistent solution was obtained for the mean flow $\bar{\phi}$, shape functions $\hat{\phi}_{mn}$, and interface height $\bar{f}$.

4. Validation

For configurations where the mean flow is exactly parallel and no streamwise variations exist, then the results of LPSE and LST should agree. Such a case can be used to validate the results of the LPSE calculations. For instance, in Fig. 4, we consider the stability of a parallel-flow mixing

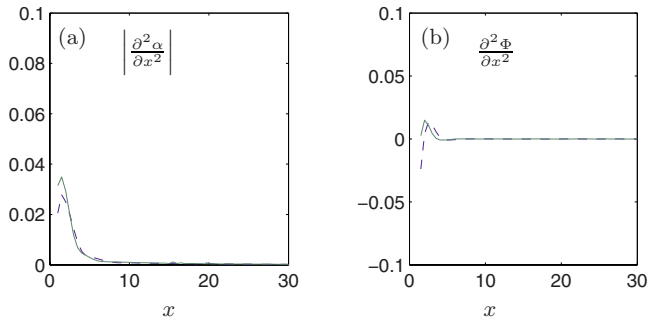

FIG. 5. (Color online) For the two-phase mixing layer with parameters $\rho_r=10$, $\mu_r=2$, Re=150, and We=300, and the second derivative (a) $|d^2\alpha/d\xi^2|$ and (b) $\partial^2\Phi/\partial\xi^2$. Liquid modes at frequencies of $\omega=0.50$ (--) and $\omega=0.75$ (—).

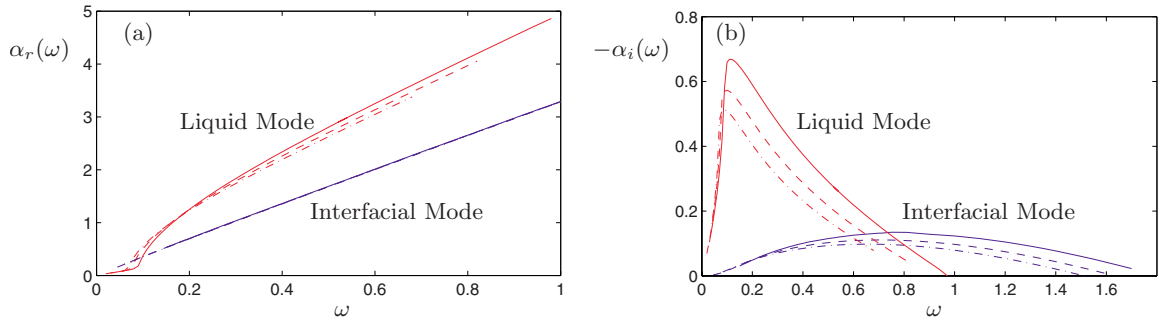

FIG. 6. (Color online) LST computed wavenumbers α_r and growth rates $-\alpha_i$ for the liquid and interfacial modes of a mixing layer with $U_2/U_1=0.03$, $\rho_r=10$, and $\mu_r=2$, at the streamwise positions $x=0$ (—), $x=5$ (--), and $x=10$ (–·–).

layer using both LPSE and LST. In this flow, the mean flow is taken to be "frozen" at $x=0$ with no normal velocity, i.e., $\bar{\mathbf{U}}=[\bar{U}(y),0]$. In addition, all streamwise derivatives of the mean flow have been eliminated.

Because any x-dependence has been eliminated from this problem, the solution to the LPSE system should not vary as the equations are marched downstream. In this case, both the shape functions $\hat{\phi}$ and wavenumbers α should remain fixed at their inlet values provided by the OS equation. As shown in Fig. 4(a), this is indeed the case, as both the LST and LPSE wavenumbers and growth rates agree throughout the entire domain. No changes are also seen between the LPSE shape functions $\hat{\phi}$ and the LST equivalents. Thus, the results of this test case verify that the LPSE system recovers the results of LST in the absence of streamwise variations.

For flows that vary in the streamwise direction, two sets of assumptions must be checked to ensure the validity of the PSE solution. The first set of assumptions presumes that the mean flow evolves slowly relative to the size of the instability wave. The second set of assumption (13), which states that higher order derivatives of $\hat{\phi}$ and α can be neglected, should be examined as well.

To examine the first set of assumptions, we compare the mean flow's rate of spreading to the typical length scale for an instability wave. In order to measure the rate at which the mean flow evolves, we use the mean momentum thickness $\theta(x)$. From θ, we can then construct an approximate length scale $L=\theta/(d\theta/dx)$ over which the mean flow evolves. For the slowly varying assumptions to hold, we require the mean flow to evolve much slower than the wavelength of the instability wave, or equivalently, the ratio $\varepsilon_{\mathrm{PSE}}=\lambda/L$ to be a small parameter, generally of the order $O(\mathrm{Re}^{-1})$. In terms of the wavenumber α_r, the requirement becomes

$$\varepsilon_{\mathrm{PSE}} \sim \frac{1}{\alpha_r \theta}\frac{d\theta}{dx} \sim O\left(\frac{1}{\mathrm{Re}}\right).$$

For the $\rho_r=10$, $\mu_r=2$, $\mathrm{Re}=150$, and $\mathrm{We}=300$ mixing layer used in Sec. III (corresponding to mean flow profiles shown in Fig. 3), the small parameter $\varepsilon_{\mathrm{PSE}}\approx 0.0044-0.0146$ for the most unstable mode, which suggests that the slowly varying mean flow assumptions are applicable.

To verify the second set of assumptions, we can also compute the magnitude of the neglected second derivative terms *a posteriori*. In Fig. 5(a), we find that $10^{-4} < |d^2\alpha/d\xi^2| < 5\times 10^{-2}$ for the liquid modes, with most of the variation occurring within the first couple steps of the PSE simulation. The changes in the wavenumber α fall within the $O(\mathrm{Re}^{-1})$ limit, and thus $d^2\alpha/d\xi^2$ can be neglected in the PSE formulation. For streamwise changes in the shape function $\hat{\phi}$, we consider the integrated shape function

$$\Phi = \int_{-\infty}^{\infty} |\hat{u}|^2 + |\hat{v}|^2 + |\hat{w}|^2 d\eta.$$

The second derivatives of Φ are shown in Fig. 5(b). Again, most of the variation occurs with the first few vorticity thicknesses downstream and quickly decays. With $|\partial^2\Phi/\partial\xi^2| < 0.04$, we find that this term can also be neglected in the derivation of the PSE, in accordance with the slowly varying assumptions.

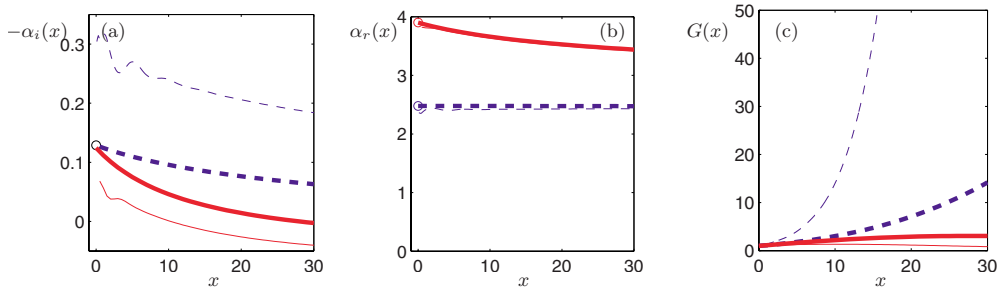

FIG. 7. (Color online) Mode competition for the mixing layer shown in Fig. 6. (a) Growth rate $-\alpha_i(x)$, (b) wavenumber $\alpha_r(x)$, and (c) amplitude gain $G_{10}(x)$ for the interfacial mode (--) and liquid mode (—) at a frequency of $\omega=0.75$. Thick lines correspond to predictions from the locally parallel LST, while thin lines from the LPSE simulations. The circles (○) correspond to the initial conditions provided by LST.

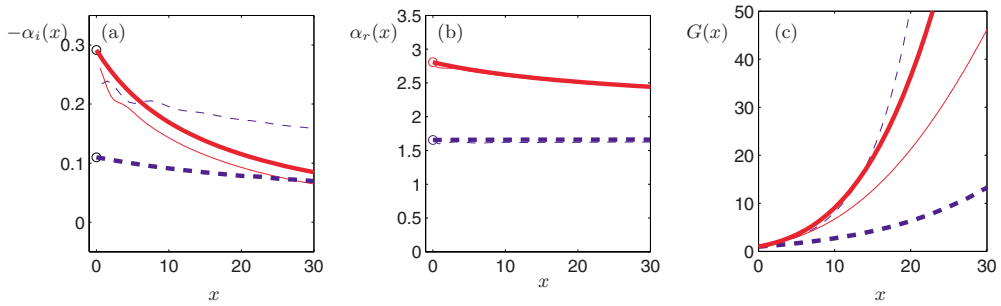

FIG. 8. (Color online) Mode competition for the mixing layer shown in Fig. 6. (a) Growth rate $-\alpha_i(x)$, (b) wavenumber $\alpha_r(x)$, and (c) amplitude gain $G_{10}(x)$ for the interfacial mode (--), liquid mode (—) at a frequency of $\omega=0.50$. Thick lines correspond to predictions from the locally parallel LST, while thin lines from the LPSE simulations. The circles (○) correspond to the initial conditions provided by LST.

III. MODE COMPETITION

To illustrate the important effects present in a nonparallel, slowly diverging mean flow, we first consider the streamwise evolution of growth rates for different mode types in a two-phase mixing layer. Prior studies by Yecko *et al.*[12] have emphasized the distinction between various viscous modes in two-phase mixing layers. They found that the most unstable mode can be either a Tollmien–Schlichting (TS)-type liquid mode or an interfacial mode, depending on the parameters of the flow. The results of locally parallel, linear stability analyses have shown that at low frequencies, the TS liquid modes generally dominate over the interfacial modes, while the reverse is true at higher frequencies.

However, local parallel-flow analyses only provide an incomplete picture regarding the mode competition between liquid and interfacial modes. The growth rates obtained by LST are valid only for a particular streamwise position, whereas in reality, the spreading of the mean flow will cause these growth rates to evolve downstream (see Fig. 6). As shown in Fig. 6, the growth rate of the most unstable frequency decreases quickly with downstream distance for liquid modes. Over the same distance, LST predicts that the decrease in the maximum growth rate is less severe for interfacial modes, which makes the outcome of mode competition unclear as the mixing layer evolves. A better description of mode competition can be supplied through a PSE analysis of the liquid and interfacial mode behavior, which will capture the effects from mean flow spreading and nonparallelism.

In the current study, we consider the growth rates of the interfacial and liquid modes of a mixing layer with the parameters $U_2/U_1=0.03$, $\rho_r=10$, $\mu_r=2$, We=300, and Re =150, whose dispersion relation is given in Fig. 6. By keeping the wave amplitudes relatively small and limiting the domain to the initial development region of the mixing layer (where $x<30$), the linear formulation suffices for the current example. In addition, moderately unstable instability waves are used in this part of the study. Although the most unstable, low frequency liquid mode could be examined using LPSE, the relatively high gain and fast growth rate introduces the possibility of finite amplitude effects. Thus, we delay the discussion of nonlinearity and the behavior further downstream until the following section and concentrate on mode competition below.

First, we consider the evolution of an interfacial mode and a liquid mode which are equally unstable (near the frequency $\omega=0.75$ in Fig. 6) at the inlet, according to locally parallel LST predictions. Once in the LPSE simulations, however, the initial guesses for the growth rate $-\alpha_i$ are adjusted to accommodate for the nonparallel effects and the presence of a streamwise varying mean flow, resulting in the interfacial mode being almost twice as unstable. As the LPSE modes evolve further downstream, we find that the growth rates for both modes slowly decrease, but whereas the liquid mode becomes stable near $x=10$, the interfacial remains unstable [see Fig. 7(a)]. The rapid decay and saturation of the liquid mode results leads to gain factor $G_{mn}(x)=|\mathcal{A}_{mn}(x)/\mathcal{A}_{mn}(0)|$, which is several orders of magnitude smaller compared to the interfacial mode [Fig. 7(b)].

In the second example we again compare the behavior of the interfacial and liquid modes, but at a lower frequency ($\omega=0.50$), where LST predicts the liquid mode to dominate over the interfacial mode according to the dispersion relation shown in Fig. 6. The corresponding PSE predictions are shown in Fig. 8. We can see that the growth rates for both modes are adjusted once in the LPSE simulation, and the liquid mode does remain slightly dominant until approximately $x=3$. The liquid mode continues to decay beyond this point, however, and the interfacial mode eventually overtakes the liquid mode downstream.

When comparing the streamwise evolution to the locally parallel LST results, we find that the presence of nonparallel

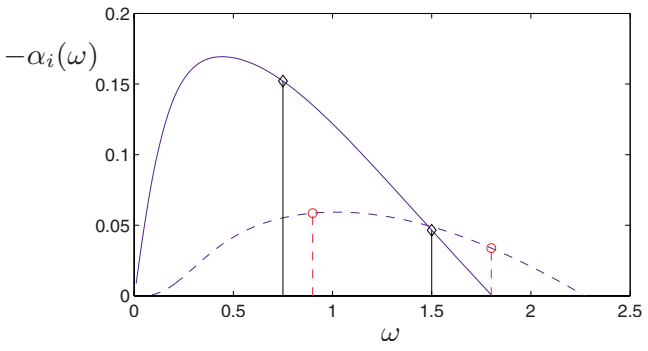

FIG. 9. (Color online) The initial dispersion relations for the interfacial (--) and liquid (—) modes in the $\rho_r=10$, $\mu_r=2$ mixing layer. The vertical spikes represent the discrete frequencies at which the mixing layers are forced. The higher harmonics with initially stable growth rates are not shown.

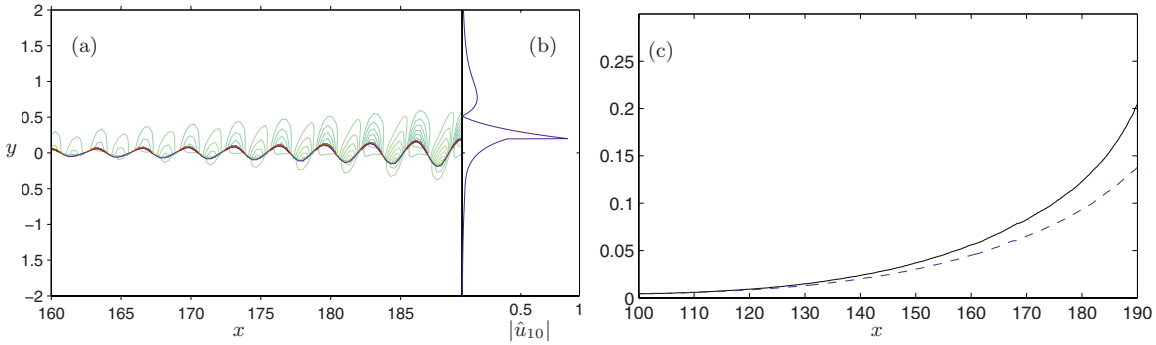

FIG. 10. (Color online) (a) Instantaneous perturbation vorticity contours for the interfacial mode forcing in the $\rho_r=10$, $\mu_r=2$ mixing layer. (b) The streamwise velocity shape function $|\hat{u}_{10}(y)|$ at $x=189$. (c) The maximum interfacial wave height $\max\{f(x,t)\}$, as computed by the nonlinear (—) and linear (--) simulations.

generally depresses the growth rate for liquid modes, and increases the growth rate for interfacial mode. This is seen in both the low frequency and high frequency examples mentioned above. Taking these observations into account, we conclude that while the predictions of locally parallel LST may be valid at a particular location of the mixing layer, capturing nonparallel effects and the streamwise evolution of the mean flow is essential to determining the downstream behavior of an interfacial wave.

IV. LINEAR AND NONLINEAR COMPUTATIONS

In the following section, we compare and contrast the effects of nonlinearity on both liquid and interfacial modes in two-phase laminar mixing layers. The results of two mixing layers are considered. The first mixing layer is similar to the case shown in Sec. III ($\rho_r=10$, $\mu_r=2$, and $\mathrm{We}=300$) with a higher velocity ratio $U_2/U_1=0.30$ in order to hasten the onset of nonlinear effects. The Reynolds number based on the velocity shear $\mathrm{Re}_{\Delta U}=\rho_1(U_1-U_2)\delta_0/\mu_1$ is defined to be $\mathrm{Re}_{\Delta U}=100$, which causes nonparallel effects to become evident early on in the mixing layer. At higher Reynolds numbers, the basic nonlinear mechanisms remain unchanged, but the extent of the linear region of the flow is increased, resulting in higher amplitude gain before the onset of nonlinearity. This case is used in the study of nonlinearity in the development of two-dimensional interfacial and liquid modes. The direct calculations of Boeck *et al.*[27] also studied low Reynolds number mixing layers with similar parameters ($\rho_r=10$ and $\mathrm{We}\approx 36-360$) and noted that the interfacial deformation in such cases eventually led to more complex ligature and droplet formation. The parameters for the second mixing layer are discussed in Secs. IV C and V.

The discrete forcing spectrum of the mixing layer is chosen to span the range of unstable frequencies at the inlet. As shown in Fig. 9, the lower frequency modes are generally selected to be near the most unstable frequency from the initial dispersion relation. Included in this forcing spectrum are additional high frequency modes, which are initially stable at the inlet. These modes are responsible for the generation of smaller scale features of the flow and are required to absorb the energy which is transferred out of the lower frequencies.

For spatially evolving mixing layers, two mechanisms can lead to the saturation of the low frequency fundamental mode. First, the spread of the mean flow will naturally dampen the growth of the mean flow, eventually causing it to become neutral and saturate. However, the fundamental mode can also quickly transition to a neutral or decaying wave as a result of the aforementioned interaction with higher harmonics. A comparison between the linear simulations (which capture the first mechanism) and nonlinear simulations (which capture both) will help distinguish the effects between the two.

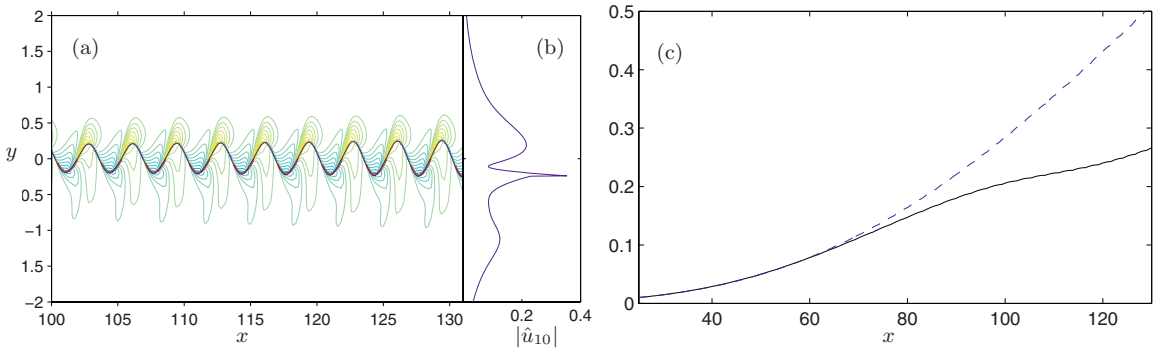

FIG. 11. (Color online) (a) Instantaneous perturbation vorticity contours for the liquid mode forcing in the $\rho_r=10$, $\mu_r=2$ mixing layer. (b) The streamwise velocity shape function $|\hat{u}_{10}(y)|$ at $x=131$. (c) The maximum interfacial wave height $\max\{f(x,t)\}$, as computed by the nonlinear (—) and linear (--) simulations.

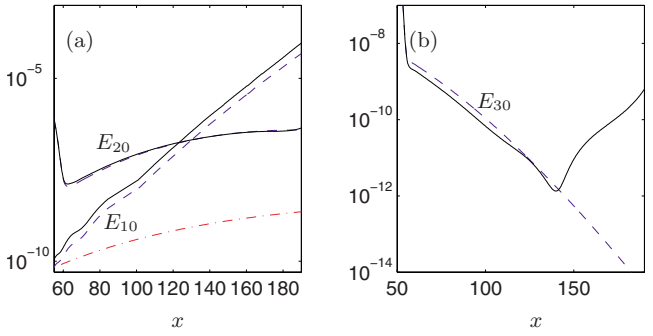

FIG. 12. (Color online) Streamwise development of the integrated modal energy $E_{mn}(x)$ for the interfacial modes in the $\rho_r=10$, $\mu_r=2$ mixing layer. The different line styles correspond to nonlinear (—), linear (--), and LST (–·–) computations.

A. Two-dimensional mixing layers

We first examine the effects of nonlinearity on the interfacial wave growth in the two-dimensional, $\rho_r=10$, $\mu_r=2$ mixing layer. For the interfacial mode, the instantaneous interfacial location $f(x,t)$ and perturbation vorticity for the mixing layer is plotted in Fig. 10(a). Immediately adjacent to the vorticity contours we also plot the streamwise velocity shape function $\hat{u}_{10}$ at the position $x=189$ and corresponding instant in time [Fig. 10(b)]. Note that the discontinuity in the shape function occurs at the physical position of the interface and not at the nominal interface height $y=0$. In Fig. 10(c) we compare the growth of the interface between the nonlinear and linear simulations. During the initial region $x<140$, the growth of the interface shows little difference between the nonlinear and the linear cases. However, further downstream the enhanced growth of the nonlinear interfacial modes is visible, where the amplitude of the interface is approximately 40% larger in the presence of nonlinearity at the position $x=190$.

An even more dramatic difference is seen in the mixing layer forced by liquid instability modes, where the presence of nonlinearity acts to suppress the growth of the interface. A corresponding set of figures for the liquid modes is shown in Fig. 11, using the same layout as in Fig. 10. Note that the spatial extent of the streamwise shape function $\hat{u}_{10}$ is larger in the liquid case than the interfacial case. As seen in Fig. 11(c), the initial growth of the interface is largely linear for $x<60$, but eventually nonlinear effects limit the maximum amplitude of the interface to $f(x,t)\approx 0.2$. Purely linear simulations predict that the liquid modes continue to grow exponentially and will ultimately reach unphysically large interface deformations. As a result of this particular example, we can see how nonlinearity plays a major role in the saturation mechanism of instability waves. The dependence of the final saturation amplitude on initial conditions is further discussed in Sec. V.

A better understanding of the interfacial wave behavior in this two-phase mixing layer can be found by examining the modal energy and amplitude development of individual instability modes. For the two-phase mixing layers in this study, we define the integrated modal energy for a particular shape function $\hat{\phi}'_{mn}=\hat{\phi}_{mn}(\xi,\eta)\mathcal{A}_{mn}(\xi)$ as

$$E_{mn}(x)=\int_{-\infty}^{\infty}\rho(|\hat{u}'_{mn}|^2+|\hat{v}'_{mn}|^2+|\hat{w}'_{mn}|^2)d\eta. \tag{23}$$

Because E_{mn} includes both streamwise varying parts of the solution ($\hat{\phi}$ and α), it is independent of the choice of the normalization (16). This provides a better measure of the instability wave's evolution than the growth rate α_i alone since α_i can change based on the normalization. In addition, the modal energy represents a physical quantity which can be used to examine nonlinear processes, such as saturation and modal interactions.

Figure 12 presents the modal energy behavior for the fundamental and first harmonic interfacial modes in the $\rho_r=10$, $\mu_r=2$ mixing layer, as calculated by the NPSE, LPSE, and parallel-flow LST. The largest differences are seen in the behavior of the fundamental mode in simulations with and without nonparallel effects. As mentioned in the earlier discussion on mode competition (Sec. III), the presence of nonparallel effects and streamwise changes greatly enhances the growth of the fundamental mode and, as a consequence, the LST computations vastly underpredict the energy content in E_{10} when compared to the PSE computations.

The inclusion of the nonlinear terms leads to two visible effects in the development of the interfacial modes. The growth of the fundamental mode is slightly enhanced, and nonlinearity also excites higher harmonics which were pre-

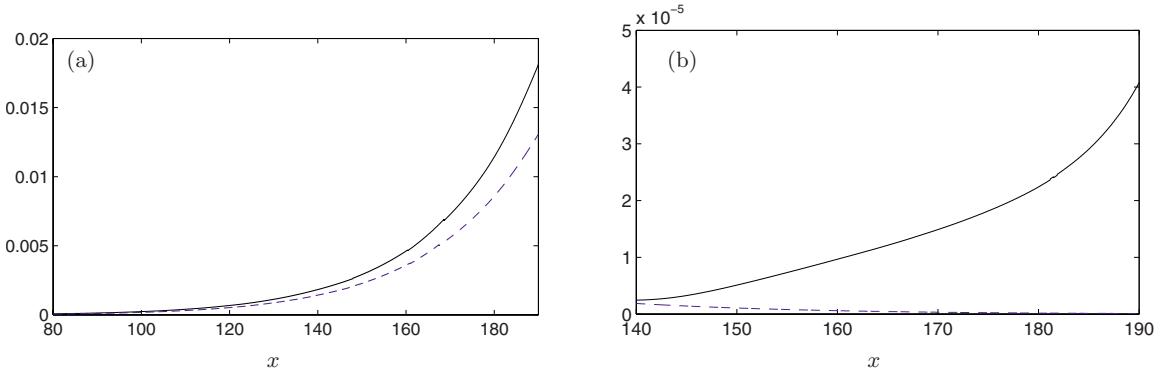

FIG. 13. (Color online) Amplitude factor $|\mathcal{A}_{mn}(x)|$ of (a) the fundamental $\hat{\phi}_{10}$ and (b) the second harmonic $\hat{\phi}_{30}$ of the interfacial mode in the $\rho_r=10$, $\mu_r=2$ mixing layer. The different line styles correspond to nonlinear (—) and linear (--) computations.

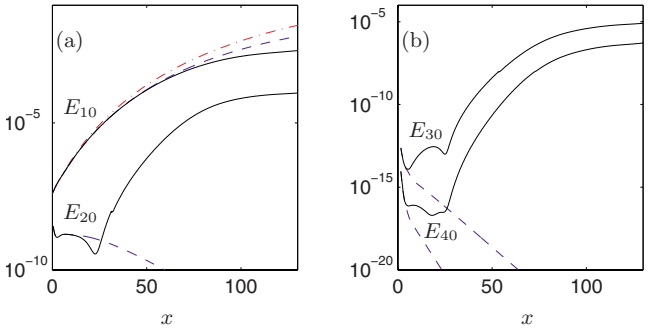

FIG. 14. (Color online) Streamwise development of the integrated modal energy $E_{mn}(x)$ for the liquid modes in the $\rho_r=10$, $\mu_r=2$ mixing layer. (a) The fundamental E_{10} and first harmonic E_{20} modes, and (b) the second E_{30} and third harmonic E_{40} modes. The different line styles correspond to nonlinear (—), linear (--), and LST (–·–) computations.

viously stable. For example, during the linear region of the flow, the second harmonic E_{30} decays exponentially, but is subsequently excited after $x>150$ [Fig. 12(b)].

The growth of the amplitude factor $\mathcal{A}_{mn}(x)$ for each instability mode reflects the same trends seen in the modal energy. In Fig. 13, the nonlinear calculations show a slightly larger growth of the fundamental mode amplitude, and the excitation of the second harmonic is clearly visible in the downstream regions of the mixing layer.

The effect of the nonlinear interactions on higher frequency instability modes can also be seen through a similar analysis of the modal energy and amplitudes for the liquid modes in the same mixing layer. In the initial development region of the mixing layer, very little difference is seen between the three formulations for the fundamental liquid mode [Fig. 14(a)]. However, further downstream of the inlet the effects of the nonparallel flow become apparent as the LST calculations of the modal energy diverge from the PSE calculations. As the instability modes reach finite amplitudes, the distinction between the linear and the nonlinear formulations also becomes visible. In the absence of nonlinearity, the fundamental mode continues to grow exponentially downstream, whereas nonlinear interactions should cause the mode to saturate at energies near $E_{mn}\approx 3\times 10^{-3}$. Some of this energy is transferred to higher harmonics of the system, such as the $\hat{\phi}_{20}$ mode, which grows several orders of magnitude as the fundamental mode reaches saturation. The observed growth and saturation of the fundamental mode is similar to the behavior of the disturbances studied by Boeck *et al.*[27] Their work also found that the interface grew exponentially, as per linear theory, before nonlinearly saturation with gains around $G\approx 10^4-10^5$. The general patterns of energy exchange and saturation are also qualitatively consistent with the results of Li *et al.*[28] and Li and Renardy.[29] A discussion of individual nonlinear effects, such as the influence of the mean flow correction on the growth of instability waves, is presented in Sec. V.

Similar to the interfacial case, nonlinear effects also play a major role in the streamwise development of previously unimportant instability modes. Although the first harmonic $\hat{\phi}_{20}$ is weakly unstable according to the dispersion relation in Fig. 9(a), it quickly becomes neutrally stable as the mean flow spreads, before being excited by the fundamental mode as mentioned above. For the $\hat{\phi}_{30}$ and $\hat{\phi}_{40}$ modes, which are initially stable at the inlet, the nonlinear interactions with other unstable modes result in their immediate excitation and eventual destabilization [see Fig. 14(b)]. While linear theory predicts that these modes simply decay and are negligible downstream [Fig. 15(b)], the results of the nonlinear theory suggest that they serve as an energy sink and could reach amplitudes comparable to the lower frequency modes. Therefore, the nonlinear amplification of the $\hat{\phi}_{20}$ or $\hat{\phi}_{40}$ mode downstream of the inlet region may be responsible for the creation of smaller scale ripples on top of an interfacial wave.

B. Energy transfer

The above discussion of modal energy considered only the total energy accumulated by each mode. Although the transfer of energy could be inferred, a more precise description of the energy transfer mechanisms occurring inside the nonlinear mixing layer is also possible. Through the energy budget analysis of Appendix D, we can define a modal energy transfer coefficient as

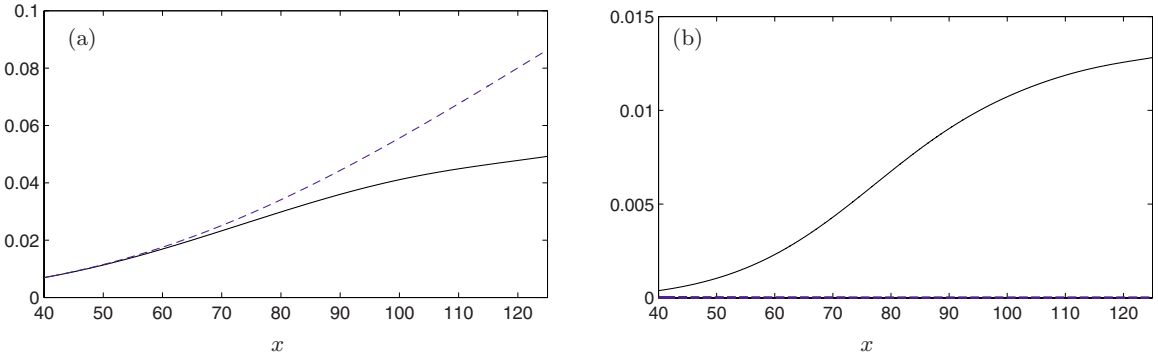

FIG. 15. (Color online) Amplitude factor $|\mathcal{A}_{mn}(x)|$ of (a) the fundamental $\hat{\phi}_{10}$ and (b) the first harmonic $\hat{\phi}_{20}$ for the liquid modes in the $\rho_r=10$, $\mu_r=2$ mixing layer. The different line styles correspond to nonlinear (—) and linear (--) computations.

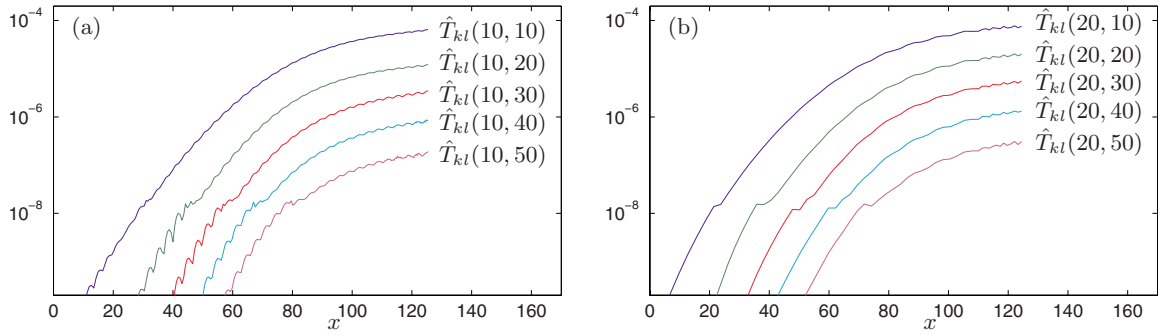

FIG. 16. (Color online) Streamwise modal energy transfer $\hat{T}_{kl}(x;mn,m'n')$ for the liquid modes in the $\rho_r=10$, $\mu_r=2$ mixing layer. (a) Energy interaction $\hat{T}_{kl}(x;10,m'n')$ between the fundamental mode (1,0) and other modes (m',n'). (b) Energy interaction $\hat{T}_{kl}(x;20,m'n')$ between the first harmonic mode (2,0) and other modes (m',n').

$$\hat{T}_{kl}(x;mn,m'n') = 2\int_{-\infty}^{\infty} |\hat{F}^*_{x,mn}\hat{u}_{m'n'}| + |\hat{F}^*_{y,mn}\hat{v}_{m'n'}| + |\hat{F}^*_{z,mn}\hat{w}_{m'n'}| d\eta. \quad (24)$$

The coefficient $\hat{T}_{kl}(x;mn,m'n')$ gives amount of energy transferred to mode (k,l) through the interaction of mode (m,n) with mode (m',n'). These energy transfer coefficients can be used in conjunction with $E_{kl}(x)$ to examine modal interactions more precisely.

In Fig. 16, we consider the modal energy interactions for the fundamental and first harmonic mode of the $\rho_r=10$, $\mu_r=2$ mixing layer discussed in the previous section. The plots of $\hat{T}_{kl}(10,m'n')$ in Fig. 16(a) illustrate the interactions of the $(m,n)=(1,0)$ mode with other (m',n') modes. The strongest energy transfer occurs when the mode is self-interacting $[\hat{T}_{kl}(10,10)]$: quadratic interactions between the fundamental (1,0) and itself will lead to energy transferred to/from the mean mode $(k,l)=(0,0)$ and the first harmonic $(k,l)=(2,0)$. The second strongest interaction $(\hat{T}_{kl}(10,20))$ leads to energy transfer to/from the fundamental (1,0) and second harmonic (3,0). The remaining interactions are weaker by several orders of magnitude. Although the coefficients $\hat{T}_{kl}(mn,m'n')$ in Eq. (24) do not provide the *direction* of energy transfer, an examination of the corresponding linear and nonlinear E_{mn} figures suggests that energy is transferred *out* of the fundamental mode *into* the mean flow and first harmonic.

Figure 16(b) shows the energy interactions of the first harmonic $(m,n)=(2,0)$. The primary interaction takes place with the fundamental $(\hat{T}_{kl}(20,10))$, which leads to energy transfer to/from the (1,0) and (3,0) modes. The second most significant interaction, $\hat{T}_{kl}(20,20)$, takes energy from the first harmonic and redistributes it to the mean flow correction (0,0) and the (4,0) mode. The higher frequency interactions are less significant, although they can still contribute to energy transfers to the (1,0) and (2,0) modes.

The results of these mixing layers suggest that nonlinear effects can serve dual purposes, both as a limiting mechanism for the growth of instability waves and can also cause the amplification of higher frequency, linearly stable modes. The general observation that initially stable, higher frequency modes are still dynamically important in predominantly linear flows is consistent with previous findings in other mixing layer studies.[42] These findings also underscore the limitation of using local, linear analysis in such a study: the dynamical evolution of two-phase instability waves cannot be accurately predicted from using the information provided by a single mode, or at a single position of the mixing layer.

C. Three-dimensional mixing layers

In this section we examine the development of three-dimensional instability waves using the second two-phase mixing layer. The parameters of this mixing layer are given by $\rho_r=2$, $\mu_r=1$, and $We=300$ using the same $Re_{\Delta U}$ as the previous mixing layer. The discrete forcing frequencies for the liquid modes, shown in Fig. 17 along with the inlet dispersion relation, encompass both low frequency, linear unstable modes and higher frequency, linearly stable modes. In this particular mixing layer, the liquid modes are the dominant instability modes, which perturb the interface, and also include a sufficiently broad spectrum of unstable spanwise harmonics, which can interact with other two- and three-dimensional modes.

The inclusion of these spanwise harmonics provides an opportunity to examine the growth of three-dimensional structures in two-phase mixing layers. In previous DNS stud-

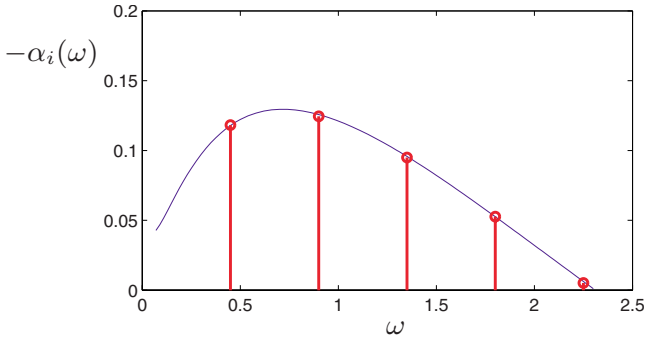

FIG. 17. (Color online) The initial dispersion relation for the liquid mode in the $\rho_r=2$, $\mu_r=1$ mixing layer, showing the $\beta=0$ forcing frequencies. The vertical spikes represent the discrete frequencies at which the mixing layers are forced. The higher harmonics with initially stable growth rates are not shown.

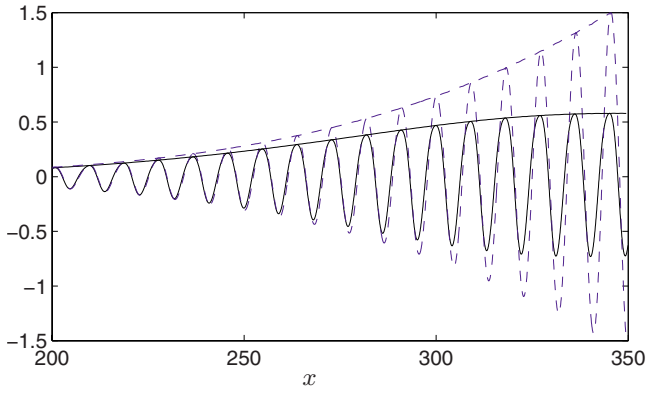

FIG. 18. (Color online) Instantaneous interfacial wave height $f(x,t)$ at $z=0$, with primary forcing at the $\hat{\phi}_{11}$ liquid mode in the $\rho_r=2$, $\mu_r=1$ mixing layer. The different line styles correspond to nonlinear (—) and linear (--) computations.

ies of single-phase, compressible and incompressible mixing layers,[45] oblique modes were observed to play a role in the development of streamwise rib vortices and the spanwise "kinking" of vortex rollers. Although the current mixing layers under consideration do not display the same vortical structures, three-dimensional effects have been shown to be important in the formation of liquid fingers and droplets in the two-fluid case.[46]

In using NPSE to simulate the $\rho_r=2$, $\mu_r=1$ mixing layer with liquid modes, two spanwise forcing schemes were employed: one in which the primary forcing mode was $\hat{\phi}_{11}$ (with spanwise wavenumber $\beta=0.10$) and the other with $\hat{\phi}_{12}$ (and $\beta=0.20$) as the primary forcing mode. Similar to the findings of Widnall,[47] we observe that the initial growth rates of the instability waves were relatively insensitive to the spanwise wavenumber at low β, but the oblique modes are responsible for the development of different spanwise structures downstream.

The comparison of the interfacial wave heights computed by the nonlinear and linear simulations is consistent with the results of the two-dimensional mixing layers in Sec. IV A. Because the linear predictions do not properly capture the saturation mechanism for instability waves, they generally tend to overestimate the growth of the interface compared to the equivalent nonlinear computations (Fig. 18). From the results of the three-dimensional mixing layers, we find that substantial energy transfer occurs between not only between modes with different harmonics but also between modes with different spanwise wavenumbers. In Figs. 19(b) and 20(c), we see that the primary energy transfer route occurs in the excitation of an immediate harmonic by the primary forcing mode (i.e., between $\hat{\phi}_{11}$ and $\hat{\phi}_{21}$ and between $\hat{\phi}_{12}$ and $\hat{\phi}_{22}$). However, in all simulations, the growth of the two-dimensional modes was still affected by the presence of the oblique modes. In Figs. 19(a) and 20(a), we find that the growth of the $\hat{\phi}_{10}$ mode is noticeably increased throughout the streamwise domain, while the $\hat{\phi}_{20}$ mode gains additional energy near the saturation point of the primary forcing mode. Additionally, in Figs. 19 and 20, it should be noted that the linear predictions are obtained from the LPSE calculations.

More prominent differences between the two forcing schemes can be observed in the three-dimensional interfacial wave patterns that develop. As illustrated in Fig. 21, forcing due to the $\hat{\phi}_{12}$ mode leads to greater spanwise variation, as expected. This forcing method produces larger height differences between adjacent wave crests in the spanwise direction and enforces the idea that higher frequency oblique modes are important to the development of liquid fingers. An examination of the three-dimensional patterns produced by the linear simulations yielded unphysically large amplitude variations in the spanwise z direction.

V. DISCUSSION OF NONLINEAR EFFECTS

From the results of Sec. IV, we have seen that nonlinear effects can both limit the growth of the instability modes, but also excite previously stable high frequency modes. In the following discussion, we use the capabilities of this formulation to examine individual nonlinear effects including the influence of the mean flow correction and the effect of the initial amplitude on the saturation mechanism.

In the context of single-fluid mixing layers, previous studies have demonstrated that appropriately accounting for the mean flow correction is essential in capturing the streamwise development of instability waves and the vortical dynamics in shear flows.[42] In the context of the two-fluid mixing layer, we can isolate the effect of the corrected mean flow by comparing simulations both with and without the mean flow forcing term $F_{x,BL}$ in Eq. (4b). For the two-dimensional $\rho_r=2$, $\mu_r=1$ mixing layer, the results can be seen in Fig. 22.

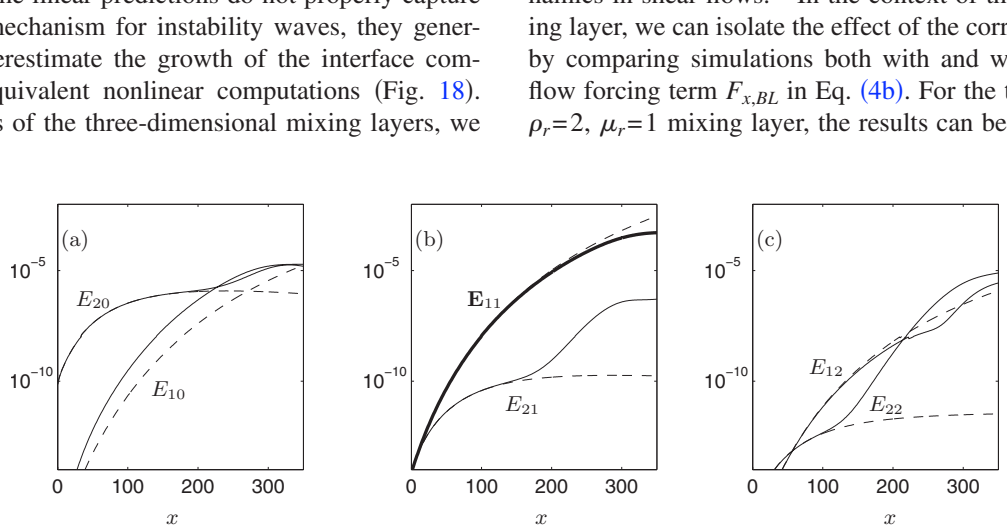

FIG. 19. Modal energy E_{mn} for liquid modes in the $\rho_r=2$, $\mu_r=1$ mixing layer, with the primary forcing originating from the $\hat{\phi}_{11}$ mode. The different line styles correspond to nonlinear (—) and linear (--) calculations, with the thick line (—) representing the primary forcing mode.

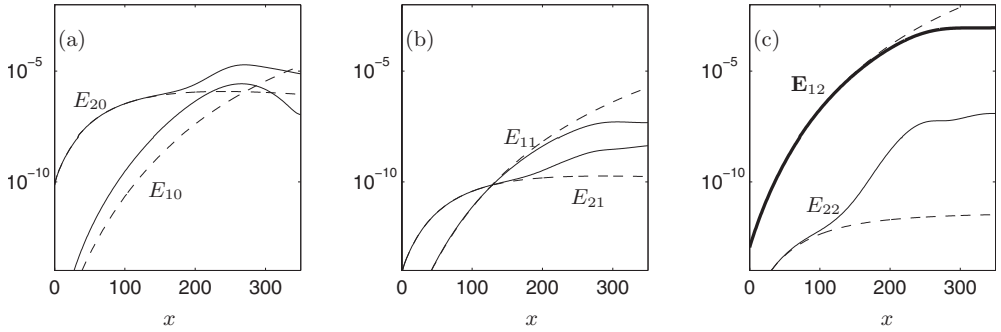

FIG. 20. Modal energy E_{mn} for liquid modes in the $\rho_r=2$, $\mu_r=1$ mixing layer, with the primary forcing originating from the $\hat{\phi}_{12}$ mode. The different line styles correspond to nonlinear (—) and linear (--) calculations, with the thick line (—) representing the primary forcing mode.

In the situation where only mode-to-mode nonlinear interactions were allowed, the eventual saturation of the fundamental mode occurred at higher amplitudes, and the first harmonic mode absorbed larger amounts of energy, when compared against the fully coupled solution with the mean flow correction. Correspondingly, the absence of the mean flow correction leads to larger wave amplitudes for the interface.

In addition, we find that the inclusion of the mean flow correction is also responsible for deformations to the mean interface location $\bar{f}(x)$. Typical linear theories, using a laminar mean flow for the mixing layer, generally specify a zero vertical velocity at the centerline, causing the mean interface to remain at $y=0$. However, in the nonparallel, spatially evolving mixing layer, the upper and lower streams experience different convective decelerations, and nonlinear interactions can introduce a nonzero mean vertical velocity at the centerline, which causes the mean interface to deform (Fig. 23). As the Weber number increases, modifications to $\bar{f}(x)$ appear earlier upstream, and even at higher levels of surface tension, the mean interface location is still displaced. This result is qualitatively consistent with the earlier work of Renardy and Renardy,[18] who also observed a long-wave modulation of the interface height in two-layer Couette–Poiseuille flow. Their formulation, however, did not incorporate a mean flow correction and also enforced interfacial boundary conditions at the nominal interface location.

The fully nonlinear instability wave formulation also allows us to explore the effects of the initial inlet amplitudes on the eventual growth of the interfacial instability modes. Previous studies on compressible mixing layers have found that the saturation amplitude of instability modes is relatively independent of the initial amplitudes used to force the discrete modes at the inlet. This observation is also consistent with the results of the two-phase mixing layers in this study. In Fig. 24, we compute the modal energies for the $\rho_r=2$, $\mu_r=1$ mixing layer using several different initial amplitudes for the fundamental mode ($\epsilon_0=1\times10^{-7}$, 2.5×10^{-7}, and 5

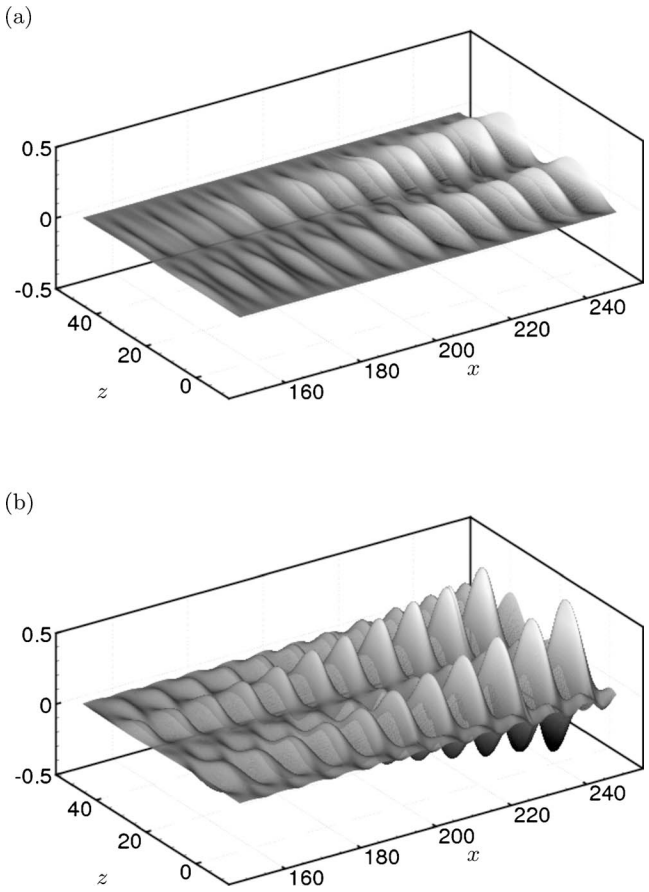

FIG. 21. Spanwise plot of instantaneous interfacial wave height $f(x,z,t)$ for liquid modes in the $\rho_r=2$, $\mu_r=1$ mixing layer. (a) Primary forcing from $\hat{\phi}_{11}$ mode. (b) Primary forcing from $\hat{\phi}_{12}$ mode.

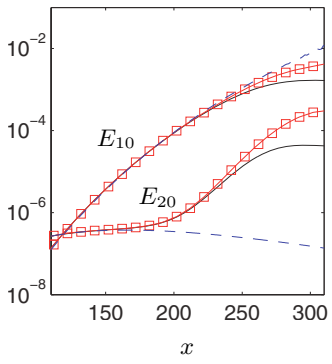

FIG. 22. (Color online) Modal kinetic energy E_{mn} for liquid modes in the $\rho_r=2$, $\mu_r=1$ mixing layer. The different line styles correspond to nonlinear calculations (—), linear calculations (--), and nonlinear calculations with no mean flow correction (⊟).

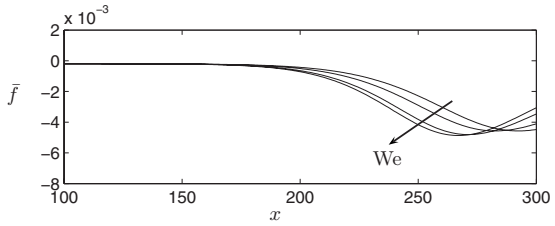

FIG. 23. The mean interface location $\bar{f}(x)$ for liquid modes in the $\rho_r=2$, $\mu_r=1$ mixing layer, with increasing curves corresponding to We $=200, 300, 600, 1000$.

$\times 10^{-7}$). Regardless of the initial amplitude, the eventual saturation amplitude of the fundamental mode was near $E_{10} \sim 10^{-3}$, although the saturation location moved upstream with increasing ϵ_0. Altering the initial amplitude of the fundamental had little effect on the eventual saturation amplitudes of higher harmonics [see Fig. 24(b)]. The onset of nonlinear growth in the higher harmonics, however, occurred more rapidly with increasing ϵ_0.

VI. CONCLUSIONS

In this investigation, we have been motivated by the need to extend the parallel-flow, linear stability analysis of two-fluid mixing layers to regimes where spatial evolution and nonlinear effects are considerable. Using a formulation based on the PSEs, we systematically investigated the influence of nonlinear mode and mean flow interactions, the mean flow correction, and finite amplitude effects on the growth of the two-fluid interface.

We find that the spatial evolution of the mixing layer and nonparallel effects play a significant role in determining the outcome of mode competition between liquid modes and interfacial modes. While parallel-flow LST can provide local predictions of the dominant mode at a given set of parameters, they fail to accurately capture the growth of modes downstream. Our results show that some interfacial modes, which are initially less unstable, can substantially amplify due to the spreading of the mean flow grow and overtake liquid modes at the same frequency.

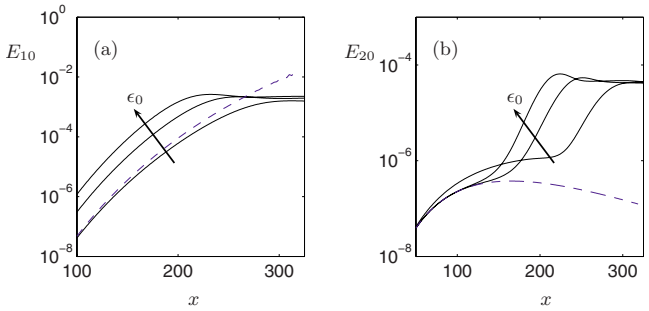

FIG. 24. (Color online) Streamwise development of the modal energy E_{mn} for the $\rho_r=2$, $\mu_r=1$ mixing layer with different inlet amplitudes for the fundamental mode. (a) Fundamental modal energy E_{10}. (b) First harmonic modal energy E_{20}. Nonlinear (—) and linear (--) computations are shown. Increasing curves correspond to inlet amplitudes of $\epsilon_0=1\times10^{-7}$, 2.5×10^{-7}, and 5×10^{-7}.

Comparisons between linear and nonlinear calculations, and parallel-flow LST showed that obtaining the correct amplitude growth for the instability waves required a proper accounting of the nonlinear modal interactions and mean flow correction. As the mixing layer develops downstream, energy is transferred from the fundamental mode to higher harmonics, which preserves or amplifies smaller scale features in the interfacial wave. Some energy is also transferred to the mean flow, which subsequently alters the mean location $\bar{f}(x,z)$ of the interface. Investigations into the sensitivity of the inlet forcing amplitudes also revealed that neither the final saturation amplitudes nor the excited amplitude of the harmonics is dependent on the initial magnitudes of the instability waves.

ACKNOWLEDGMENTS

This research was supported by a Marie Curie International Incoming Fellowship within the 7th European Community Framework Programme. Further support was provided by the Imperial Marshall Sherfield Fellowship and the U.K. Engineering and Physical Sciences Research Council (Grant No. EP/F034997).

APPENDIX A: MEAN FLOW SIMILARITY SOLUTION

The similarity solution to the two-fluid mixing layer problem was derived by Lock[48] and is available in Ref. 40. It was recommended that the details of the solution be included here for completeness. This self-similar solution provides the inlet and free-stream boundary conditions for the mean flow described in Sec. II B. The Blasius-type similarity variable χ for each individual stream is defined as

$$\chi_j \equiv y\sqrt{\frac{U_1}{2x\mu_j/\rho_j}},$$

where the index j denotes either the upper $(j=1)$ or lower $(j=2)$ stream. The similarity function $\psi(\chi)$ is related to the nondimensional velocity in each stream by

$$\psi_j'(\chi) \equiv \frac{\bar{U}_j(\chi)}{U_1}.$$

Substitution of these definitions into the boundary layer equations yields a Blasius-type ordinary differential equation for each stream

$$\psi_j''' + \psi_j\psi_j'' = 0. \tag{A1}$$

At the upper and lower limits, the velocities should approach the two free-stream velocities, leading to the following boundary conditions:

$$\psi_1'(+\infty) = 1, \quad \psi_2'(-\infty) = U_2/U_1. \tag{A2}$$

The interfacial conditions are satisfied by imposing the following equalities on ψ at $\chi=0$:

$$\psi_1(0)=\psi_2(0),\quad \psi_1'(0)=\psi_2'(0),\quad \psi_1''(0)=\sqrt{\frac{\rho_2\mu_2}{\rho_1\mu_1}}\psi_2''(0). \tag{A3}$$

In our work, the boundary value problems (A1)–(A3) are solved using a shooting method and adaptive Runge–Kutta integration. Once the solution ψ_j is determined, the self-similar velocities in physical space can be found through the relations $\bar{U}_j^{SS}=U_1\psi_j'$, $\bar{V}_j^{SS}=\sqrt{\nu_j U_1/(2x)}(\chi\psi_j'-\psi_j)$ and translated to physical coordinates,

$$\bar{U}^{SS}(x,y)=\begin{cases}\bar{U}_1^{SS}[\chi(x,y)], & \chi\geq 0,\\ \bar{U}_2^{SS}[\chi(x,y)], & \chi<0,\end{cases}$$

$$\bar{V}^{SS}(x,y)=\begin{cases}\bar{V}_1^{SS}[\chi(x,y)], & \chi\geq 0,\\ \bar{V}_2^{SS}[\chi(x,y)], & \chi<0.\end{cases}$$

At the virtual origin of the mixing layer, the sudden mating of the high-speed and low-speed streams gives rise to a discontinuity in the velocity profile. The discontinuity leads to a singularity in the self-similar solution at this location. To avoid this singularity, we initialize the mixing layer at a distance far downstream of the virtual origin. Hence, all results in this work have been presented using the coordinate $x=x^*-x_0$, where x^* originates at the virtual origin and x_0 is the distance from the virtual origin to the location where $\delta_\omega(x_0)=\delta_0=1$. The vorticity thickness $\delta_\omega(x)$ of the mixing layer is defined by

$$\delta_\omega(x)=\frac{U_1-U_2}{|d\bar{U}/dy|_{\max}}.$$

APPENDIX B: PSE OPERATOR

For the LPSE operator

$$\mathcal{L}_{mn}=-i\omega_m\mathbf{G}+i\alpha_{mn}\mathbf{A}+\mathbf{B}\frac{\partial}{\partial\eta}+\mathbf{C}\frac{\partial^2}{\partial\eta^2}+i\beta_n\mathbf{D}+\mathbf{E}+\mathbf{M}\frac{\partial}{\partial\xi}+\frac{\partial\alpha_{mn}}{\partial\xi}\mathbf{N}$$

acting on the vector $\hat{\phi}_{mn}=[\hat{u}_{mn}\ \hat{v}_{mn}\ \hat{w}_{mn}\ \hat{p}_{mn}]^T$, the matrices **A**, **B**, **C**, **D**, **E**, **G**, **M**, and **N** are given by

$$\mathbf{A}=\begin{pmatrix}\rho\bar{U}&0&0&1\\0&\rho\bar{U}&0&0\\0&0&\rho\bar{U}&0\\1&0&0&0\end{pmatrix},\quad \mathbf{B}=\begin{pmatrix}\rho\bar{V}&0&0&0\\0&\rho\bar{V}&0&1\\0&0&\rho\bar{V}&0\\0&1&0&0\end{pmatrix},\quad \mathbf{C}=-\frac{\mu}{\mathrm{Re}}\begin{pmatrix}1&0&0&0\\0&1&0&0\\0&0&1&0\\0&0&0&0\end{pmatrix},$$

$$\mathbf{D}=\begin{pmatrix}\rho\bar{W}&0&0&0\\0&\rho\bar{W}&0&0\\0&0&\rho\bar{W}&1\\0&0&1&0\end{pmatrix},\quad \mathbf{E}=\begin{pmatrix}\rho\frac{\partial\bar{U}}{\partial\xi}+\frac{\mu}{\mathrm{Re}}(\alpha_{mn}^2+\beta_n^2)&\rho\frac{\partial\bar{U}}{\partial\eta}&\rho\frac{\partial\bar{U}}{\partial\zeta}&0\\ \rho\frac{\partial\bar{V}}{\partial\xi}&\rho\frac{\partial\bar{V}}{\partial\eta}+\frac{\mu}{\mathrm{Re}}(\alpha_{mn}^2+\beta_n^2)&\rho\frac{\partial\bar{V}}{\partial\zeta}&0\\ \rho\frac{\partial\bar{W}}{\partial\xi}&\rho\frac{\partial\bar{W}}{\partial\eta}&\rho\frac{\partial\bar{W}}{\partial\eta}+\frac{\mu}{\mathrm{Re}}(\alpha_{mn}^2+\beta_n^2)&0\\ 0&0&0&0\end{pmatrix},$$

$$\mathbf{G}=\begin{pmatrix}\rho&0&0&0\\0&\rho&0&0\\0&0&\rho&0\\0&0&0&0\end{pmatrix},\quad \mathbf{N}=-\frac{i\mu}{\mathrm{Re}}\begin{pmatrix}1&0&0&0\\0&1&0&0\\0&0&1&0\\0&0&0&0\end{pmatrix},\quad \mathbf{M}=\begin{pmatrix}\rho\bar{U}-2i\alpha_{mn}\frac{\mu}{\mathrm{Re}}&0&0&\Omega\\0&\rho\bar{U}-2i\alpha_{mn}\frac{\mu}{\mathrm{Re}}&0&0\\0&0&\rho\bar{U}-2i\alpha_{mn}\frac{\mu}{\mathrm{Re}}&0\\1&0&0&0\end{pmatrix}.$$

In our calculations, the matrices have been simplified by neglecting the spanwise mean flow, i.e., $\bar{W}=0$, and by assuming that the mean flow is independent of the spanwise coordinate, i.e., $\bar{\phi}=\bar{\phi}(x,y)$ only.

APPENDIX C: INLET FORCING AND LST FORMULATION

The solution to the parallel-flow, linear stability problem provides the inlet conditions to the PSE problem and is the basis for comparison with LPSE results in Secs. III and IV. At the starting location $\xi=\xi_0$, the mean flow is assumed to be parallel and nonspreading so that $\bar{U}=\bar{U}(\eta)$ and $\bar{V}=0$. The perturbation equations (7) can then be reduced to the spatial OS equation, a single ordinary differential equation for the vertical velocity perturbation $\hat{v}$,

$$i\ \mathrm{Re}\frac{\rho}{\mu}[M(\mathrm{D}^2-k^2)-M'']\hat{v}_{mn}=(\mathrm{D}^2-k^2)^2\hat{v}_{mn}, \tag{C1}$$

where $\mathrm{D}=d/d\eta$, $k^2=\alpha^2+\beta^2$, and $M(\eta)=\alpha\bar{U}(\eta)-\omega$. Because the amplitudes of the perturbations are assumed to be small at the inlet, the interfacial conditions

$$\left[\!\left[\frac{\partial\hat{v}_{mn}}{\partial\eta}\right]\!\right]-\left[\!\left[\frac{\partial M}{\partial\eta}\right]\!\right]\frac{\hat{v}_{mn}}{M}=0,\quad [\![\hat{v}_{mn}]\!]=0, \tag{C2}$$

$$\left[\!\left[-\hat{p}_{mn}+2\mu\frac{\partial\hat{v}_{mn}}{\partial\eta}\right]\!\right]=-\frac{ik^2\hat{v}_{mn}}{\mathrm{We}M},$$

$$\left[\!\left[\mu\left(\frac{\partial^2\hat{v}_{mn}}{\partial\eta^2}+\left(k^2-\frac{M''}{M}\right)\hat{v}_{mn}\right)\right]\!\right]=0 \tag{C3}$$

are applied at the location $\eta=\bar{f}(\xi_0)=0$. In the free-stream $\eta\rightarrow\pm\infty$, we apply the boundary conditions

$$i\ \mathrm{Re}\frac{\rho}{\mu}[M_{1,2}(\mathrm{D}^2-k^2)]\hat{v}_{mn}-(\mathrm{D}^2-k^2)^2\hat{v}_{mn}=0.$$

In addition to the OS equation (C1), the Squire equation for the vorticity $\hat{\Theta}_{mn}$ can also be formulated as

$$\left[\mathrm{D}^2-\left(k^2+\frac{i\rho M}{\mu}\mathrm{Re}\right)\right]\hat{\Theta}_{mn}=\frac{i\rho}{\mu}\mathrm{Re}\ \ \beta\bar{U}'\hat{v}_{mn}$$

with the interfacial conditions $[\![\hat{\Theta}_{mn}]\!]=0$ and $[\![\mu\partial\hat{\Theta}/\partial\eta]\!]=0$. Once the solutions to the OS and Squire equations are found, the other linear stability eigenfunctions $\hat{u}^{\mathrm{OS}}_{mn}$, $\hat{w}^{\mathrm{OS}}_{mn}$, and $\hat{p}^{\mathrm{OS}}_{mn}$ can be determined from linear combinations of $\hat{v}^{\mathrm{OS}}_{mn}$ and $\hat{\Theta}^{\mathrm{OS}}_{mn}$ and their derivatives. The shape function at the inlet of the PSE solution can then be constructed as $\hat{\phi}_{mn}(\xi_0,\eta)=[\hat{u}^{\mathrm{OS}}_{mn}\ \hat{v}^{\mathrm{OS}}_{mn}\ \hat{w}^{\mathrm{OS}}_{mn}\ \hat{p}^{\mathrm{OS}}_{mn}]^T$, where the eigenmodes are scaled such that $\max\{|\hat{u}_{mn}|,|\hat{v}_{mn}|,|\hat{w}_{mn}|\}=1$. As mentioned in Sec. II C 2, the inlet perturbations in the time domain can be written as

$$\tilde{\phi}(\xi=0,\eta,\zeta,\tau)=\sum_{m,n}\epsilon_{mn}\hat{\phi}^{\mathrm{OS}}_{mn}(\eta)e^{-im\omega_0\tau+i\beta_n\zeta},$$

where ϵ_{mn} were generally less than 0.1% of the free-stream velocity U_1.

APPENDIX D: ENERGY TRANSFER

Following the analysis of Chu,[49] a mechanical energy balance equation can be derived by considering the perturbation equation (7b). When multiplied by the perturbation velocities $\tilde{u}_i$,

$$\tilde{u}_i\left\{\rho\left(\frac{\partial\tilde{u}_i}{\partial t}+\tilde{u}_j\frac{\partial\bar{U}_i}{\partial x_j}+\bar{U}_j\frac{\partial\tilde{u}_i}{\partial x_j}\right)-\frac{\partial\tilde{\sigma}_{ij}}{\partial x_j}\right\}=\tilde{u}_i\tilde{F}_i, \tag{D1}$$

the following conservation equation for the kinetic energy $\rho\tilde{u}_i\tilde{u}_i/2$ can be written:

$$\frac{\bar{\mathrm{D}}}{\mathrm{D}t}\left(\frac{\rho\tilde{u}_i\tilde{u}_i}{2}\right)+\rho\tilde{u}_i\tilde{u}_j\frac{\partial\bar{U}_i}{\partial x_j}-\frac{\partial}{\partial x_j}(\tilde{u}_i\tilde{\sigma}_{ij})+\tilde{\sigma}_{ij}\frac{\partial\tilde{u}_i}{\partial x_j}=\tilde{u}_i\tilde{F}_i. \tag{D2}$$

Here, we assume the perturbation stress tensor can be written as $\tilde{\sigma}_{ij}=\tilde{P}\delta_{ij}+\tilde{\tau}_{ij}=\tilde{P}\delta_{ij}+\mu(\partial\tilde{u}_i/\partial x_j+\partial\tilde{u}_j/\partial x_i)$ and the operator $\bar{\mathrm{D}}/\mathrm{D}t=\partial/\partial t+\bar{U}_j\partial/\partial x_j$. When Eq. (D2) is integrated over the entire domain Ω, and the boundary conditions in which the velocities $\tilde{u}_i$ and stresses $\tilde{\sigma}_{ij}$ vanish at infinity have been applied, we arrive at the balance equation

$$\frac{\bar{\mathrm{D}}\tilde{E}}{\mathrm{D}t}+\tilde{\mathcal{P}}+\tilde{\Phi}=\tilde{\mathcal{I}}+\tilde{\mathcal{T}}. \tag{D3}$$

The energy $\tilde{E}$, production $\tilde{\mathcal{P}}$, dissipation $\tilde{\Phi}$, interfacial energy $\tilde{\mathcal{I}}$, and energy transfer $\tilde{\mathcal{T}}$ terms in Eq. (D3) have been defined as

$$\tilde{E}=\int\frac{\rho}{2}\tilde{u}_i\tilde{u}_i d\Omega,\quad \tilde{\mathcal{P}}=\int\rho\tilde{u}_i\tilde{u}_j\frac{\partial\bar{U}_i}{\partial x_j}d\Omega,$$

$$\tilde{\Phi}=\int\tilde{\tau}_{ij}\frac{\partial\tilde{u}_i}{\partial x_j}d\Omega,\quad \tilde{\mathcal{I}}=[\![\tilde{u}_i\tilde{\sigma}_{ij}\hat{n}_j]\!],\quad \tilde{\mathcal{T}}=\int\tilde{F}_i\tilde{u}_i d\Omega,$$

respectively. The production and dissipation terms are analogous to the terms found in the kinetic energy budgets for turbulent flows. The interfacial energy term $\tilde{\mathcal{I}}$ can be separated into contributions from the work done by shear stress and normal stress components, as done by Boomkamp and Miesen.[10] For instance, if the interface remains relatively flat, then the tangential and normal energy components take the form

$$\tilde{\mathcal{I}}_{\mathrm{TAN}}=\left[\!\left[\tilde{u}\mu\left(\frac{\partial\tilde{u}}{\partial y}+\frac{\partial\tilde{v}}{\partial x}\right)\right]\!\right],\quad \tilde{\mathcal{I}}_{\mathrm{NOR}}=\left[\!\left[\tilde{v}\left(-\tilde{p}+2\mu\frac{\partial\tilde{v}}{\partial y}\right)\right]\!\right].$$

However, of particular interest is the energy transfer term $\tilde{\mathcal{T}}$, which is the main source of energy redistribution among modes when the nonlinear forcing term is present in Eq. (7b). We can express $\tilde{\mathcal{T}}$ in terms of the individual frequency components by considering the modal expansion

$$\tilde{\mathcal{T}} = \int \left(\sum_{m,n} \hat{\mathcal{F}}_{mn} e^{-i\omega_m t + i\beta_n z} \right) \cdot \left(\sum_{m',n'} \hat{\mathbf{u}}_{m'n'} e^{-i\omega_{m'} t + i\beta_{n'} z} \right) d\Omega$$

$$= \int \sum_{m,n} \sum_{m',n'} \hat{\mathcal{F}}_{mn} \cdot \hat{\mathbf{u}}_{m'n'} e^{-i(\omega_m + \omega_{m'})t + i(\beta_n + \beta_{n'})z} d\Omega$$

$$= \int \sum_{k,l} \hat{\mathcal{T}}_{kl} e^{-i\omega_k t + i\beta_l z} d\Omega .$$

If we define $\hat{\mathsf{T}}_{kl}(mn,m'n') = \hat{\mathcal{F}}_{mn} \cdot \hat{\mathbf{u}}_{m'n'}$ with the relations $\omega_k = \omega_m \pm \omega_{m'}$ and $\beta_l = \beta_n \pm \beta_{n'}$, then the individual frequency components $\hat{\mathcal{T}}_{kl}$ can be expressed as

$$\hat{\mathcal{T}}_{kl} = \sum_{mn,m'n'} \hat{\mathsf{T}}_{kl}(mn;m'n'), \tag{D4}$$

where the summation occurs over all values of (m,n) and (m',n') which fit the criteria above. Thus, the modal energy transfer coefficients $\hat{\mathsf{T}}_{kl}(mn,m'n')$ can be interpreted as the amount of energy transferred to mode (k,l) through the interaction of mode (m,n) with mode (m',n'). Because of the symmetry of shape functions, the interaction of between the (m,n) and (m',n') modes can affect up to four other modes: $(k,l)=(m+m',n+n')$, $(m-n',n+n')$, $(m+m',n-n')$, $(m-m',n-n')$. To examine the streamwise development of the modal energy transfer, we consider the positive definite quantity $\hat{T}_{kl}(x;mn,m'n')$,

$$\hat{T}_{kl}(x;mn,m'n') = 2\int_{-\infty}^{\infty} |\hat{F}^*_{x,mn}\hat{u}_{m'n'}| + |\hat{F}^*_{y,mn}\hat{v}_{m'n'}| + |\hat{F}^*_{z,mn}\hat{w}_{m'n'}| d\eta, \tag{D5}$$

which has been multiplied by 2 to ensure compatibility with the modal energy definition in Eq. (23),

$$E_{mn}(x) = \int_{-\infty}^{\infty} \rho(|\hat{u}'_{mn}|^2 + |\hat{v}'_{mn}|^2 + |\hat{w}'_{mn}|^2) d\eta.$$

[1] J. W. Miles, "On the generation of surface waves by shear flows," J. Fluid Mech. **3**, 185 (1957).
[2] J. W. Miles, "The hydrodynamic stability of a thin film of liquid in uniform shearing motion," J. Fluid Mech. **8**, 593 (1960).
[3] C. S. Yih, "Instability due to viscosity stratification," J. Fluid Mech. **27**, 337 (1967).
[4] A. P. Hooper and W. G. C. Boyd, "Shear-flow instability at the interface between two viscous fluids," J. Fluid Mech. **128**, 507 (1983).
[5] E. J. Hinch, "A note on the mechanism of the instability at the interface between two shearing fluids," J. Fluid Mech. **144**, 463 (1984).
[6] Y. Renardy and D. D. Joseph, "Couette flow of two fluids between concentric cylinders," J. Fluid Mech. **150**, 381 (1985).
[7] Y. Renardy and D. D. Joseph, "Oscillatory instability in a Bénard problem of two fluids," Phys. Fluids **28**, 788 (1985).
[8] S. G. Yiantsios and B. G. Higgins, "Linear stability of plane Poiseuille flow of two superposed fluids," Phys. Fluids **31**, 3225 (1988).
[9] A. P. Hooper and W. G. C. Boyd, "Shear-flow instability due to a wall and a viscosity discontinuity at the interface," J. Fluid Mech. **179**, 201 (1987).
[10] P. A. M. Boomkamp and R. H. M. Miesen, "Classification of instabilities in parallel two-phase flow," Int. J. Multiphase Flow **22**, 67 (1996).
[11] H. H. Hu and D. D. Joseph, "Lubricated pipelining: Stability of core-annular flow. Part 2," J. Fluid Mech. **205**, 359 (1989).
[12] P. Yecko, S. Zaleski, and J.-M. Fullana, "Viscous modes in two-phase mixing layers," Phys. Fluids **14**, 4115 (2002).
[13] P. Yecko and S. Zaleski, "Transient growth in two-phase mixing layers," J. Fluid Mech. **528**, 43 (2005).
[14] M. J. South and A. P. Hooper, "Linear growth in two-fluid plane Poiseuille flow," J. Fluid Mech. **381**, 121 (1999).
[15] T. L. van Noorden, P. A. M. Boomkamp, M. C. Knaap, and T. M. M. Verheggen, "Transient growth in parallel two-phase flow: Analogies and differences with single-phase flow," Phys. Fluids **10**, 2099 (1998).
[16] A. P. Hooper and R. Grimshaw, "Nonlinear instability at the interface between two viscous fluids," Phys. Fluids **28**, 37 (1985).
[17] Y. Renardy, "Weakly nonlinear behavior of periodic disturbances in two-layer Couette–Poiseuille flow," Phys. Fluids A **1**, 1666 (1989).
[18] M. Renardy and Y. Renardy, "Derivation of amplitude equations and analysis of sideband instabilities in two-layer flows," Phys. Fluids A **5**, 2738 (1993).
[19] M. R. King and M. J. McCready, "Weakly nonlinear simulation of planar stratified flows," Phys. Fluids **12**, 92 (2000).
[20] M. Sangalli, C. T. Gallagher, D. T. Leighton, H.-C. Chang, and M. J. McCready, "Finite-amplitude waves at the interface between fluids with different viscosity: Theory and experiments," Phys. Rev. Lett. **75**, 77 (1995).
[21] M. Sangalli, M. J. McCready, and H.-C. Chang, "Stabilization mechanisms of short waves in stratified gas–liquid flow," Phys. Fluids **9**, 919 (1997).
[22] B. Khomami and K. C. Su, "An experimental/theoretical investigation of interfacial instabilities in superposed pressure-driven channel flow of Newtonian and well characterized viscoelastic fluids: Part I: Linear stability and encapsulation effects," J. Non-Newtonian Fluid Mech. **91**, 59 (2000).
[23] B. Khomami, Y. Renardy, K. C. Su, and M. A. Clarke, "An experimental/theoretical investigation of interfacial instabilities in superposed pressure-driven channel flow of Newtonian and well-characterized viscoelastic fluids: Part II. Nonlinear stability," J. Non-Newtonian Fluid Mech. **91**, 85 (2000).
[24] P. Lombardi, V. D. Angelis, and S. Banerjee, "Direct numerical simulation of near-interface turbulence in coupled gas-liquid flow," Phys. Fluids **8**, 1643 (1996).
[25] M. Fulgosi, D. Lakehal, S. Banerjee, and V. DeAngelis, "Direct numerical simulation of turbulence in a sheared air-water flow with a deformable interface," J. Fluid Mech. **482**, 319 (2003).
[26] A. Alexakis, A. C. Calder, L. J. Dursi, R. Rosner, J. W. Truran, B. Fryxell, M. Zingale, F. X. Timmes, K. Olson, and P. Ricker, "On the nonlinear evolution of wind-driven gravity waves," Phys. Fluids **16**, 3256 (2004).
[27] T. Boeck, J. Li, E. Lopez-Pages, P. Yecko, and S. Zaleski, "Ligament formation in sheared liquid–gas layers," Theor. Comput. Fluid Dyn. **21**, 59 (2007).
[28] J. Li, Y. Y. Renardy, and M. Renardy, "A numerical study of periodic disturbances on two-layer Couette flow," Phys. Fluids **10**, 3056 (1998).
[29] J. Li and Y. Renardy, "Numerical study of flows of two immiscible liquids at low Reynolds number," SIAM Rev. **42**, 417 (2000).
[30] D. Gueyffier, J. Li, A. Nadim, R. Scardovelli, and S. Zaleski, "Volume-of-fluid interface tracking with smoothed surface stress methods for three-dimensional flows," J. Comput. Phys. **152**, 423 (1999).
[31] M. Sussman, P. Smereka, and S. Osher, "A level set approach for computing solutions to incompressible two-phase flow," J. Comput. Phys. **114**, 146 (1994).
[32] M. Herrmann, "A balanced force refined level set grid method for two-phase flows on unstructured flow solver grids," J. Comput. Phys. **227**, 2674 (2008).
[33] H. Ding, P. D. Spelt, and C. Shu, "Diffuse interface model for incompressible two-phase flows with large density ratios," J. Comput. Phys. **226**, 2078 (2007).
[34] M. Gorokhovski and M. Herrmann, "Modeling primary atomization," Annu. Rev. Fluid Mech. **40**, 343 (2008).
[35] F. P. Bertolotti, T. Herbert, and P. R. Spalart, "Linear and nonlinear stability of the Blasius boundary layer," J. Fluid Mech. **242**, 441 (1992).
[36] T. Herbert, "Parabolized stability equations," Annu. Rev. Fluid Mech. **29**, 245 (1997).
[37] M. R. Malik and C. L. Chang, "Nonparallel and nonlinear stability of supersonic jet flow," Comput. Fluids **29**, 327 (2000).
[38] M. J. Day, N. N. Mansour, and W. C. Reynolds, "Nonlinear stability and structure of compressible reacting mixing layers," J. Fluid Mech. **446**, 375 (2001).
[39] P. Huerre and P. A. Monkewitz, "Local and global instabilities in spatially developing flows," Annu. Rev. Fluid Mech. **22**, 473 (1990).

[40]F. M. White, *Viscous Fluid Flow* (McGraw-Hill, New York, 1991).
[41]C. A. J. Fletcher, *Computational Techniques for Fluid Dynamics 2* (Springer-Verlag, Berlin, 1991).
[42]L. C. Cheung and S. K. Lele, "Linear and non-linear processes in two-dimensional mixing layer dynamics and sound radiation," J. Fluid Mech. **625**, 321 (2009).
[43]H. Haj-Hariri, "Characteristics analysis of the parabolized stability equations," Stud. Appl. Math. **92**, 41 (1994).
[44]F. Li and M. R. Malik, "On the nature of the PSE approximation," Theor. Comput. Fluid Dyn. **8**, 253 (1996).
[45]M. M. Rogers and R. D. Moser, "The three-dimensional evolution of a plane mixing layer: The Kelvin–Helmholtz rollup," J. Fluid Mech. **243**, 183 (1992).
[46]A. Lozano, F. Barreras, G. Hauke, and C. Dopazo, "Longitudinal instabilities in an air-blasted liquid sheet," J. Fluid Mech. **437**, 143 (2001).
[47]R. T. Pierrehumbert and S. E. Widnall, "The two- and three-dimensional instabilities of a spatially periodic shear layer," J. Fluid Mech. **114**, 59 (1982).
[48]R. C. Lock, "The velocity distribution in the laminar boundary layer between parallel streams," Q. J. Mech. Appl. Math. **4**, 42 (1951).
[49]B. T. Chu, "On the energy transfer to small disturbances in fluid flow (part I)," Acta Mech. **1**, 215 (1965).